Evaluation of a deterministic Boltzmann solver for radiation therapy dose calculations involving high-density hip prostheses

by

Samantha AM Lloyd
BSc, Thompson Rivers University, 2009

A Thesis Submitted in Partial Fulfillment of the
Requirements for the Degree of

MASTER OF SCIENCE

in the Department of Physics and Astronomy

University of Victoria

Evaluation of a deterministic Boltzmann solver for radiation therapy dose calculations involving high-density hip prostheses

by

Samantha AM Lloyd
BSc, Thompson Rivers University, 2009

Supervisory Committee

Dr. W. Ansbacher, Co-supervisor
(Department of Physics and Astronomy)
(British Columbia Cancer Agency - Vancouver Island Centre)

Dr. A. Jirasek, Co-supervisor
(Department of Physics and Astronomy)

Dr. P. Basran, Member
(Department of Physics and Astronomy)
(British Columbia Cancer Agency - Vancouver Island Centre)

Supervisory Committee

Dr. W. Ansbacher, Co-supervisor
(Department of Physics and Astronomy)
(British Columbia Cancer Agency - Vancouver Island Centre)

Dr. A. Jirasek, Co-supervisor
(Department of Physics and Astronomy)

Dr. P. Basran, Member
(Department of Physics and Astronomy)
(British Columbia Cancer Agency - Vancouver Island Centre)

ABSTRACT

Acuros® External Beam (Acuros XB) is a new radiation dose calculation algorithm available as part of Varian Medical Systems' radiotherapy treatment planning system, ECLIPSE™. Acuros XB calculates dose distributions by finding the deterministic solution to the linear Boltzmann transport equation which governs the transport of particles or radiation through matter. Among other things, Acuros XB claims an ability to accurately model dose perturbations due to increased photon and electron scatter within a high-density volume, such as a hip prosthesis. Until now, the only way to accurately model high-density scatter was with a Monte Carlo simulation which gives the stochastic solution to the same transport equation, but is time and computationally expensive. In contrast, Acuros XB solves the transport equation at time scales appropriate for clinical use.

An evaluation of Acuros XB for radiation dose calculations involving high-density objects was undertaken using EGSnrc based Monte Carlo as the benchmark. Calculations were performed for geometrically ideal virtual phantoms, water tank phantoms containing cylindrical steel rods and hip prostheses, and for a clinical prostate treatment plan involving a unilateral prosthetic hip. The anisotropic analytical algorithm

(AAA), a convolution-superposition algorithm used for treatment planning at the British Columbia Cancer Agency's Vancouver Island Center, was also used to illustrate the limitations of current radiotherapy planning tools. In addition, to verify the qualitative properties of dose perturbations due to high-density volumes, film measurements were taken and compared to Monte Carlo, Acuros XB and AAA data.

Dose distributions calculated with Acuros XB agree very well with distributions calculated with Monte Carlo. γ-analyses performed at 2% and 2 mm using Monte Carlo as the reference dose were within tolerance for 92–99% of voxels considered. AAA, on the other hand, was within tolerance for 61–97% of voxels considered under the same γ-constraints. For the clinical prostate plan, AAA produced localized dose underestimates that were absent when calculated by Acuros XB. As well, both Monte Carlo and Acuros XB showed very good agreement with the film measurements, while AAA showed large discrepancies at and beyond the location of measured dose perturbations.

Acuros XB has been shown to handle does perturbations due to high-density volumes as well as Monte Carlo, at clinically appropriate time scales, and better than the current algorithm used for treatment planning at the Vancouver Island Center.

Contents

List of Tables

List of Figures

Acknowledgments

My sincerest thanks go to my supervisory committee for all their feedback and support. This work would have been impossible without the guidance and infinite patience of Will Ansbacher and Karl Bush. Thanks to Sergei Zavgorodni for the Monte Carlo help and the hard questions, and to everyone else at the BC Cancer Agency's Vancouver Island Centre - physicists, students and support staff - for setting examples of passion, dedication and excellence. You've all given me a lot to live up to.

Additional thanks to Dr. Reft and the AAPM for allowing me to use a figure from their Task Group Report, and to Varian Medical Systems for providing Eclipse and Acuros XB. This work has been supported, in part, by an Alexander Graham Bell Canada Graduate Scholarship from the Natural Sciences and Engineering Research Council of Canada.

Chapter 1

Introduction

Approximately half of the 45% of Canadian men and 40% of Canadian women who develop cancer during their lifetime will receive radiation therapy as part of their treatment [1, 2]. Medical physicists and radiotherapy treatment planners use sophisticated dose calculation algorithms to simulate the distribution of radiation dose for a treatment plan to ensure treatment efficacy and patient safety. Acuros® External Beam (Acuros XB) is a novel dose calculation algorithm available from the commercial vendor, Varian Medical Systems [3]. Among other things, Acuros XB should be an improvement over current clinical algorithms for calculations involving high-density implants. Until now, there has been no reliable, clinically appropriate method of accurately modeling the dose perturbations that arise due to increased photon and electron scatter in high-density materials.

The aim of this work is to evaluate the accuracy of Acuros XB for dose calculations involving high-density objects, specifically hip prostheses, by comparison with Monte Carlo. The following chapter provides a brief overview of radiation therapy physics, hip prostheses and their impact on radiotherapy planning, and a summary of the thesis scope.

1.1 Radiation Therapy

Radiation therapy, or radiotherapy, is the targeted delivery of highly energetic photons or particles to a specific patient volume with the purpose of destroying cancerous cells within healthy tissue. It can be an internal or an external treatment, making use of radioactive isotopes that emit energetic photons or particles as they decay, or by producing and delivering energetic photons or particles with a medical accelerator. Used alone, radiation therapy is capable of curing many cancers and can be safely used in concert with other therapies such as surgery and pharmaceuticals. In addition, palliative radiotherapy can greatly reduce the pain associated with tumour growth in late stages of the disease, significantly improving quality-of-life for patients receiving end-of-life care.

Figure 1.1: Varian Clinac 21EX, the model of clinical linear accelerator used for radiation therapy at the BC Cancer Agency's Vancouver Island Centre.

The first radiation therapy treatments took place shortly after the discoveries of radium and the X-ray in the 1890's. These therapies involved surface moulds of radioactive isotopes and keV photon therapies which were used for decades even though they were ineffective for all but the most superficial lesions [4, 5]. Megavoltage external beam therapies began in 1937 as radiation therapy evolved from a palliative therapy into a curative form of cancer treatment [6, 7]. The introduction of the first cobalt-60 therapy units in Saskatchewan and Ontario in 1951 followed by the first clinical linear accelerator used in London in 1953 set the stage for the external beam mega-voltage therapies that are not only still in use, but are the dominant technique for therapeutic radiation delivery [6, 8, 9]. Consequently, external-beam, mega-voltage radiation therapy is the focus of this work. An example of a medical linear accelerator used at the BC Cancer Agency's Vancouver Island Centre (VIC) is shown in Figure 1.1.

Today, spectral 6 MV and 18 MV photon beams are delivered with millimetre precision at escalating prescribed doses and in more complex geometries than ever before. The precision and quality of these treatments are limited by the daily reproducibility of patient position in the radiation field, the ability to locate and delineate the tumour volume on a planning image and the accuracy with which planners can predict the resulting dose distribution within a patient. Accurate treatment planning is a critical precursor to ensuring maximum tumour coverage while mitigating the severity of side effects and probability of secondary cancers caused by normal tissue exposure. What follows are descriptions of the treatment planning process and the algorithms used to simulate radiotherapy delivery.

1.1.1 Radiation Therapy Treatment Planning

Radiotherapy planning is done, for the most part, using sophisticated image rendering and dose calculation software packages called treatment planning systems. The process begins with a medical image, usually an x-ray computed tomography (CT) image such as that in Figure 1.2, on which a team of radiation oncologists and radiotherapy planners, or dosimetrists, delineate the volumes to be treated and critical organs to be spared. Based on these contours, the dosimetrist uses the planning system to set the positions and properties of external photon beams and employs a dose calculation algorithm to model the resulting dose distribution. An example of a treatment plan and dose distribution is shown in Figure 1.3. The planning team may evaluate the quality of the plan based on the simulated dose distribution and make necessary modifications until a satisfactory distribution is produced. Acceptance criteria for a treatment plan depend on the delivery technique used but often include a homogeneous target dose as well as upper dose limits for proportional volumes of at-risk organs, for example, no more than 20% of a particular organ may receive more than 30 Gy. Once an acceptable treatment plan has been approved by the radiation on-

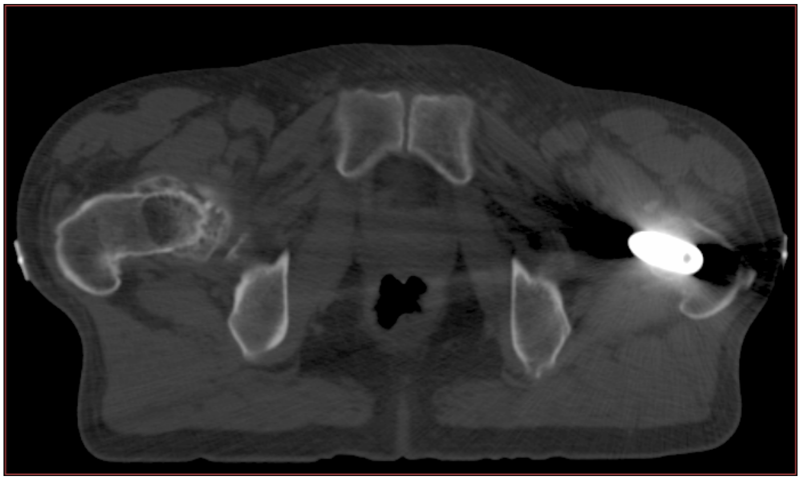

Figure 1.2: Slice of a CT image used for radiotherapy planning.

cologist and, if necessary, a medical physicist, it is transfered to the linear accelerator control console for delivery.

The radiation therapy plan that a patient ultimately receives is dependent on the modeling algorithm's representation of the resulting dose distribution. Consequently, the quality and efficacy of a radiotherapy plan hinges on the ability of a dose calculation algorithm to accurately model dose deposition. Naturally, medical physicists are constantly improving existing algorithms and employing new techniques to bridge the gap between radiotherapy models and reality.

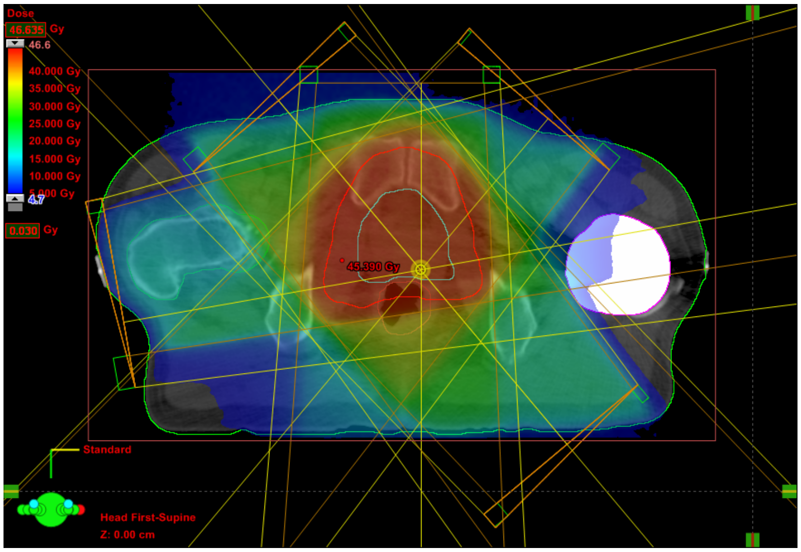

Figure 1.3: Example of a radiation therapy treatment plan and calculated dose distribution overlaid on a CT image.

1.1.2 Dose Calculation Algorithms

Modern dose calculation algorithms generally fall into two categories: convolution-superposition or Boltzmann-solvers. Both types of algorithm base their calculations on the material properties contained in the planning image and the physical interactions that govern the transport of radiation through media, though some algorithms are better at modeling these interactions than others. The dominant particle interactions in radiotherapy include the photoelectric effect, where a photon interacts with an electron, imparting all of its energy to the secondary electron; Compton scattering, where a photon interacts with an electron imparting some energy to the secondary electron while retaining part of its initial energy; pair production, where a photon interacts with an atomic nucleus to produce and electron-positron pair; bremsstrahlung radiation, where an electron interacts with an atomic nucleus to produce a photon; and electron scattering. These interactions are discussed in greater detail in Chapter 2. [8, 10]

Convolution-superposition algorithms model the attenuation of primary photons through a volume of interest before using one or more measurement or Monte Carlo generated scatter kernels to determine the resulting dose deposition [5]. Because much of the calculation or measurement is done beforehand, convolution algorithms are characteristically fast and well-suited to clinical environments. The solutions they provide are based on acceptable approximations for most patient volumes and treatment techniques.

Boltzmann-solvers are algorithms that directly solve the Linear Boltzmann Transport Equation (LBTE), a set of partial differential equations that govern the transport of particles or radiation through matter. Monte Carlo is the best known Boltzmann-solver, providing a stochastic solution to LBTE. A random number generator is used to sample the properties and interactions of particles as they are transported explicitly through a volume of interest. Monte Carlo simulations are generally accepted as the most accurate model of particle transport and dose deposition, however, because the history of each primary and secondary particle is modeled explicitly, calculations are characteristically slow and usually reserved for research applications. Acuros XB is the newest commercial, medical purpose Boltzmann-solver, providing a deterministic solution to the LBTE. Chapter 2 provides a detailed discussion of the Boltzmann-solvers and of convolution-superposition algorithms. [3]

1.2 High Density Implants

Dental fillings, metal plates, portacaths and pacemakers are just a few examples of high-density implants that may be found in the human body. The presence of a high-density object in a radiation field causes significant perturbations to the resulting dose distribution, so high-density implants are a matter of concern in radiotherapy treatment planning. Due to their size and inevitable involvement in pelvic irradiation, hip prostheses are of particular interest to planners and physicists.

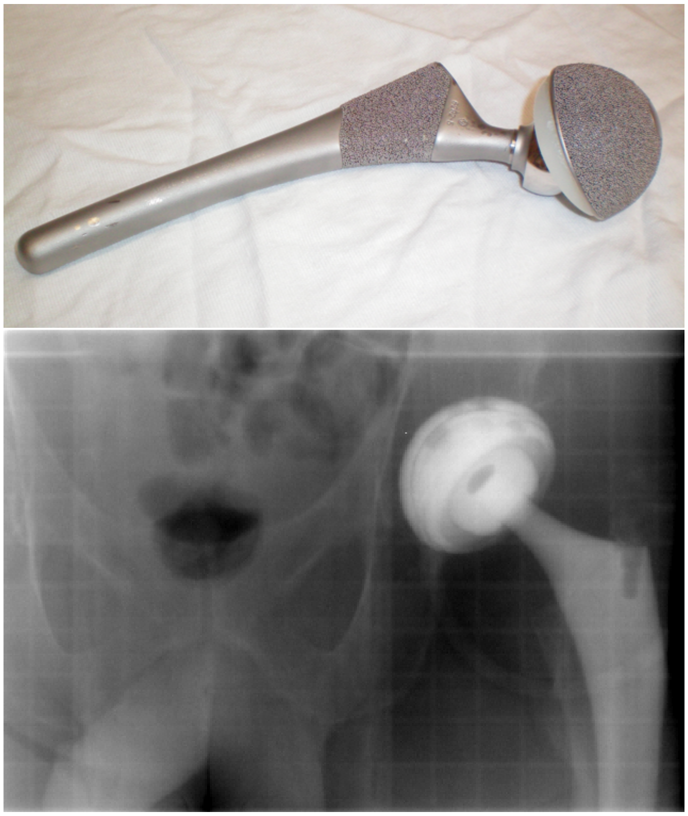

Figure 1.4: Photograph (top) and radiograph (bottom) of typical hip prostheses.

Hip prostheses have three parts: a femoral stem, head and acetabular cup. Some patients have only the stem while others have all three parts. The head is typically made of a polyethylene core with a metal shell of titanium alloy, steel or Co-Cr-Mo. The stem and head are typically made of titanium alloy, steel or Co-Cr-Mo and may be solid or hollow. [11] A typical hip prosthesis and radiograph of an implanted prothesis are displayed in Figure 1.4. CT images of high-density objects are notoriously corrupted by streaking and shadowing artifacts that result from the complete attenuation of imaging x-rays by the high-density material, as demonstrated in Figure 1.2.

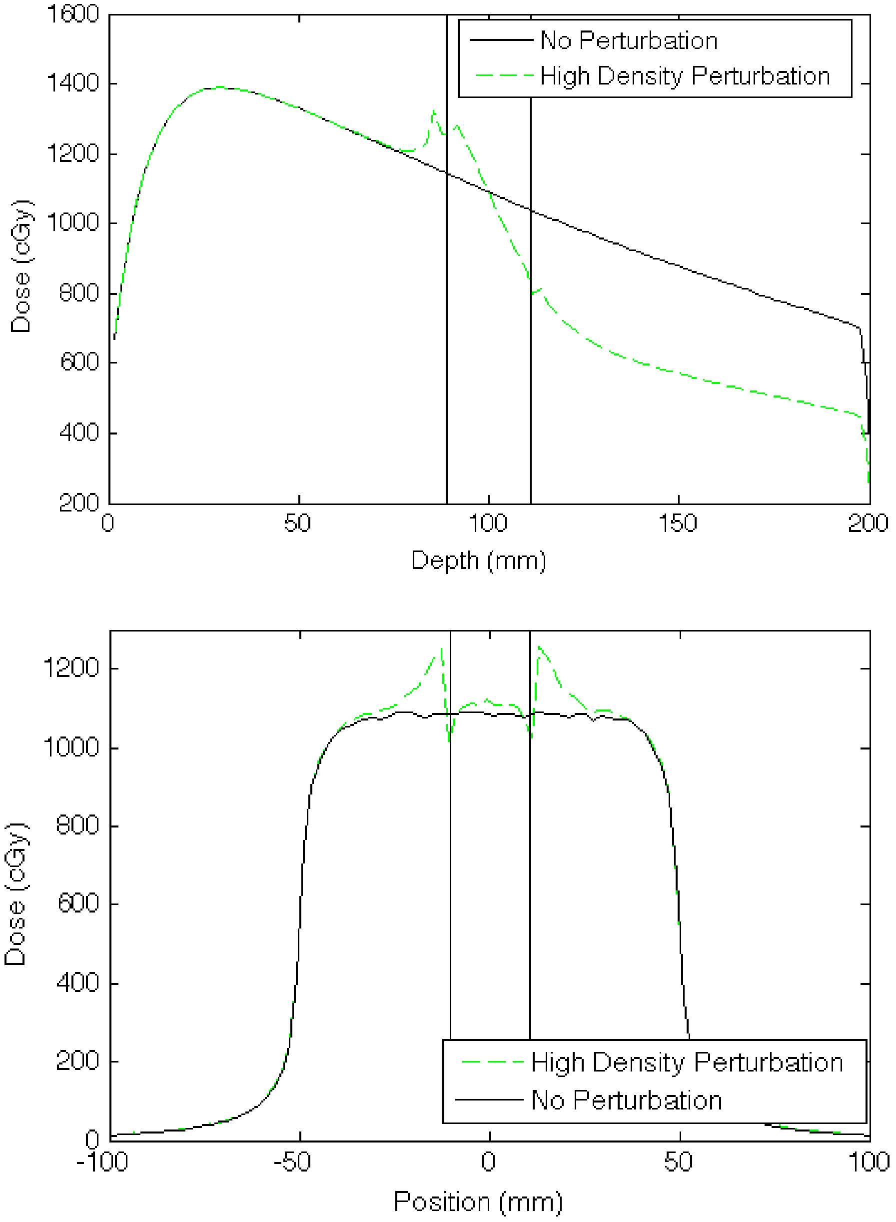

Figure 1.5: Example of a depth dose (top) and dose profile (bottom) perturbed by the presence of a high-density object. Both data sets were generated using EGSnrc based Monte Carlo.

Figure 1.5 displays the depth dose (top) and dose profile (bottom) plots for a square 18 MV field through a phantom generated by Monte Carlo simulations. The black curves are data for a homogeneous phantom while the green curves show the perturbations that result from a square high-density inhomogeneity, contained within the vertical black lines. The presence of the inhomogeneity causes an increase in photon attenuation, increasing the number of secondary photons and electrons which, in turn, interact more frequently within the high-density object. This has a number of effects: the equilibrium of forward-backward and right-left scattered electrons breaks down at the material interfaces producing dose build-down and build-up effects, the increased number and scattering of electrons in the implant means an increase in the number of electrons leaving the high-density object causing dramatic dose peaks on the top and lateral surfaces of the inhomogeneity, and the increased attenuation of primary photons results in lower dose beyond the high-density region.

Monte Carlo systems are known to model high-density scatter very accurately [11]. Unfortunately, Monte Carlo calculations are too computationally expensive for clinical use. The convolution-superposition algorithms used in clinics for daily treatment planning are capable of correcting for some inhomogeneities, but these corrections are insufficient when dealing with very high-density materials such as titanium alloy or steel and grossly underestimate the resulting dose perturbations. Pelvic patients who have had one or both hips replaced with prostheses often receive an optimal treatment technique that has been coarsely adapted to avoid treating through the prosthesis and corrected, approximately, to account for dose shadowing and increased interface doses.

1.3 Thesis Scope

In November 2010, Varian Medical Systems received clearance from the US Food and Drug Administration to market their new dose calculation algorithm, Acuros XB. Based on the general purpose radiation transport modeling system, Attila®, first developed at Los Alamos National Laboratory in Los Alamos, New Mexico, Acuros XB has been modified and optimized for radiation therapy planning calculations [3, 12].

Four teams of physicists world-wide, including a team at VIC, were selected to perform the pre-release verification of Acuros XB version 11.0 as implemented in ECLIPSE™, Varian's treatment planning system. These evaluations have been underway for just over a year and are producing extremely encouraging results [13, 14]. As part of this investigation, and as the objective of this thesis, the ability of Acuros

XB to accurately model dose perturbations due to the presence of a high-density object is evaluated. This evaluation is done, principally, against EGSnrc-based Monte Carlo using single, open fields incident on tissue volumes containing high-density geometries of varying complexity. In addition, a set of radio-chromic film measurements are included to qualitatively verify the shape of the high-density perturbation with depth. To illustrate the impact of high-density perturbations on clinical work, an anonymized prostate treatment plan is re-calculated with Acuros XB and Monte Carlo and evaluated.

The current dose calculation algorithm used for treatment planning at VIC is the anisotropic analytical algorithm (AAA), one of the leading convolution-superposition calculation techniques available. AAA has been extensively evaluated and has performed very well for most clinical cases [15, 16]. The inclusion of AAA data in this work is to highlight current algorithm limitations and the advantages of a clinical algorithm designed to handle high-density perturbations.

Chapter 2 will discuss, in detail, the photon and particle interactions that take place during radiation therapy and the ways in which the dose calculation algorithms attempt to model them. As well, image acquisition and modification for treatment planning and radio-chromic film dosimetry will be covered.

Chapter 3 outlines the implementations of Acuros XB, Monte Carlo and AAA and their associated user-defined settings. As well, Chapter 3 includes descriptions of all the experimental set ups, from film measurement calibrations to prostate contours, concluding with an explanation of the γ-analysis which will be used in Chapter 4.

Chapter 4 presents all of the measured and calculated experimental data, as well as analyses, while Chapter 5 is a discussion of the results and their significance. Chapter 6 will conclude with an overall assessment of Acuros XB and its performance, as well as remaining concerns and considerations.

Chapter 2

Theory

This chapter will provide the necessary theoretical background to proceed with the experimental details of this research. The physics of therapeutic photon and electron interactions and the principles behind the dose modeling algorithms Acuros XB, Monte Carlo and AAA are presented, followed by an introduction to CT imaging, pixelation effects and radiotherapy planning contouring. Finally, the basics of radiochromic dosimetry, used for measurements in later chapters, are covered.

2.1 Particle Interactions

To facilitate a thorough discussion of high-density perturbations on dose distribution, the physical interactions that lead to radiation dose deposition are presented here. Because therapeutic photons generally have a maximum energy of 21 MeV, only those photon and particle interactions that take place at energies less than 21 MeV are discussed. As well, exotic beams involving protons or heavier particles have been omitted.

2.1.1 Photon Interactions

Photoelectric Effect

The photoelectric effect is the process by which a photon with energy $h\nu$ is absorbed by an atom which, as a result, emits an electron with energy $h\nu - E_B$ where E_B is the binding energy of the ejected electron. This process leaves the atom in an excited state and it relaxes by emitting a characteristic x-ray or subsequent Auger electron. The photoelectric effect is most likely to occur when the photon's energy is slightly greater than the electron's binding energy and low energy interactions tend to produce photo-electrons ejected at right angles while higher energy interactions will eject photo-electrons in a forward direction.

The mass attenuation coefficient for photoelectric interactions varies as Z^3 for high-Z media and as $Z^{3.8}$ for low-Z media. For low-Z materials the photoelectric effect is dominant at energies below 200 keV and varies approximately with energy as $1/(h\nu)^3$. [8]

Coherent and Incoherent Scattering

The most common photon interaction at therapeutic energies is scattering by electrons. There are two types of photon scatter: coherent and incoherent. Coherent, or Rayleigh scattering, involves the deflection of a photon off atomic electrons during which none of the photon's energy is converted to electron kinetic energy. Atomic electrons, subject to the electric field of an incident photon, are set into vibrational motion and the oscillations of each electron emit a particular wavelength of radiation that combine to form the wave of the incident photon, but traveling in a new direction. Rayleigh scattering is primarily forward directed and has little impact on photons with energy greater than 100 keV.

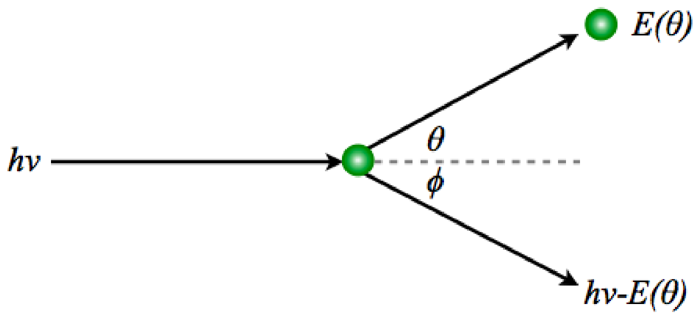

Figure 2.1: A single electron undergoes a Compton scattering event.

The most significant interaction for photons between 200 keV and 5 MeV in tissue-like material is incoherent scattering, or Compton scattering, during which a photon interacts with an atomic electron and is scattered at a new trajectory while the electron is ejected with kinetic energy imparted by the incident photon. Figure 2.1

shows a schematic of a Compton scattering event. The photon has initial energy $h\nu$ before colliding with the electron. Because the electron's binding energy is greatly exceeded by the energy of the incident photon, it is treated as a free electron. The electron is ejected from its orbit at some angle θ with energy $E(\theta)$ while the photon is scattered at a corresponding angle ϕ with energy $h\nu - E(\theta)$.

The Klein-Nishina formula is used by EGSnrc Monte Carlo, discussed in Section 3.1, to determine the Compton cross section and is given per unit solid angle:

$$\frac{d\sigma}{d\Omega} = \frac{r_0^2}{2}\left(1+\cos^2\theta\right)\left\{\frac{1}{1+\alpha(1-\cos\theta)}\right\}^2\left\{1+\frac{\alpha^2(1-\cos\theta)^2}{[1+\alpha(1-\cos\theta)](1+\cos^2\theta)}\right\} \tag{2.1}$$

where $\alpha = h\nu/m_0c^2$, and m_0c^2 is the rest mass of an electron. [8]

If the scattered electron is emitted in the direction of the incident photon, the scattered photon will be emitted at 180° and the electron will have the maximum energy possible for a Compton electron. Conversely, a scattered electron will receive the least possible energy if the incident photon grazes by and continues nearly straight forward, emitting the scattered electron at nearly 90°. Compton interactions are nearly independent of atomic number and decrease with increasing energy. [8]

Pair Production

Pair production is the conversion of energy to mass that results when a photon is subject to the strong field of an atomic nucleus and becomes an electron-positron pair. The photon must have energy of at least 1.022 MeV to comprise the rest masses of the charged particles. Any additional energy held by the photon is distributed between the electron and positron as kinetic energy. Because the atomic nucleus plays a part in this interaction it receives a very small portion of the photon's momentum; consequently, the momentum of the electron does not uniquely predict the momentum of the positron and vice-versa. If the incident photon has an energy of at least 2.04 MeV, it may interact in the field of an orbital electron to the same end, with the addition of an ejected atomic electron. This less common process is called triplet production as it produces a total of three charged particles.

A positron will propagate through and ionize matter in the same manner as an electron until it slows enough to annihilate with a free electron and produce two 0.511 MeV photons which are ejected at 180° from one another. If the positron has some remaining kinetic energy when it annihilates, the angle will be nearly 180°.

The incidence of pair-production interactions increases rapidly with increasing energy once the 1.022 MeV threshold has been met and the mass attenuation coefficient increases approximately with atomic number. Pair production is the dominant photon interaction at energies in excess of 5 MeV. [8]

Characteristic x-rays & Auger Electrons

Characteristic x-rays, or fluorescence x-rays, are the photons emitted when an atomic orbital vacancy is filled by an electron from a higher orbital shell. The energy of a characteristic x-ray is equal to the difference in binding energies between the orbital levels and is unique to atomic number. If a characteristic x-ray is absorbed by an outer orbit electron, that electron is ejected with the energy of the characteristic x-ray less the binding energy of the electron and is called an Auger electron. [8]

2.1.2 Electron Interactions

The dose perturbations of interest in this work are due, primarily, to the increase in number and scattering of secondary electrons [17]. Electron interactions, including radiative scattering, are covered here.

Soft & Hard Collisions

By convention, when an electron interacts with another electron it is assumed that the electron that emerges with the greatest energy is the original electron: the maximum energy transfer between electrons is half the incident energy. An electron-electron interaction is depicted in Figure 2.2. As a free electron approaches a bound electron their fields interact causing the bound electron to become excited or even ejected, ionizing the atom [10].

The impact parameter, b, determines the magnitude of energy transfer from the free electron to the bound electron. While b is greater than the atomic radius, r, the transfer of energy is typically small and is inversely proportional to b^2; this interaction is called a soft collision [8]. When b is approximately r, however, large energy transfers occur as the electrons collide and the binding energy of the atomic electron is negligible [18]. These high energy interactions are called hard collisions and their resulting secondary electrons are referred to as delta rays [10].

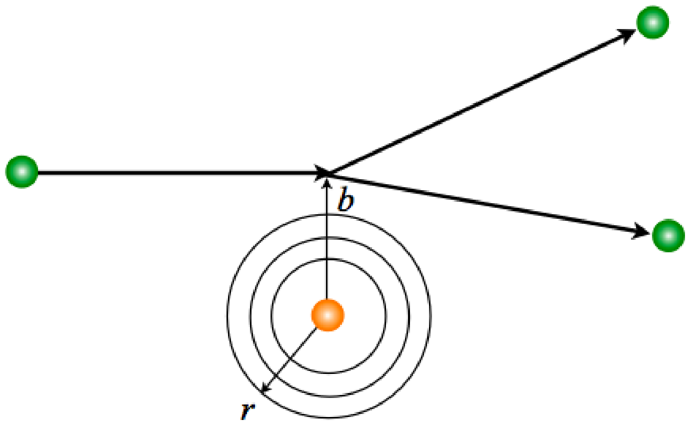

Figure 2.2: Schematic depiction of a soft electron interaction with another electron.

Bremsstrahlung Radiation

If the impact parameter, b, is much smaller than r the incident electron interacts mainly with the atomic nucleus. In most cases, the electron interacts elastically with the electric field of the nucleus and is scattered with no energy loss. Two to three precent of the time, however, the electron decelerates in the nuclear electric field and is scattered inelastically, losing energy in the form of a radiative photon called bremsstrahlung radiation, or breaking radiation. Bremsstrahlung radiation is insignificant for low-density media and for electrons with energy less than 10 MeV. [8, 10]

The Bethe-Heitler cross-section for bremsstrahlung radiation, which is used by EGSnrc Monte Carlo, is given by

$$S_r = \frac{1}{137}\left(\frac{e^2}{m_0 c^2}\right)^2 \frac{N_A Z^2}{A}\left(E + m_0 c^2\right)\bar{B}_r \tag{2.2}$$

where N_A is Avogadro's constant and $\bar{B}_r$ is slowly varying function of Z and E corresponding to $\frac{16}{3}$ for $E << 0.5$ MeV, approximately 6 for $E = 1$ MeV, 12 for $E = 10$ MeV and 15 for $E = 100$ MeV. [10]

2.2 Dose Calculation Algorithms

Historically, dose computation algorithms have been either correction-based or model-based. Correction-based algorithms start with the distribution of dose delivered to a phantom and require corrections for contour irregularities, media inhomogeneities, beam modifiers and variations in the distance from the beam source [5]. These calculations can be done largely by hand, and while they are useful for making ballpark estimates of dose distributions, they are no longer used for clinical treatment planning if model-based algorithms are available.

Model-based algorithms simulate dose deposition based on the actual volume of interest, usually a patient CT [5]. Having potential for greater accuracy and expediency resulting from the use of a computer, model-based algorithms are the standard technique for performing treatment planning calculations. The algorithms of consequence to this work can be subdivided into convolution-superposition algorithms and Boltzmann-solvers, described below.

2.2.1 Convolution-Superposition Algorithms

Convolution algorithms model dose deposition in a two step process. In the first step, primary photons are transported to their first interaction site where TERMA, or total energy released per unit mass, is assigned. TERMA is the product of the primary energy fluence and the mass attenuation coefficient for the material of interest. In the second step, a convolution kernel is applied to model the dose scatter that results from secondary photon and electron intereactions. The resulting dose, $D\left(\vec{r}\right)$, is a convolution of the TERMA, T, and a dose kernel, A,

$$D(\vec{r}) = T * A. \tag{2.3}$$

A dose kernel is a matrix that represents dose deposition by scattered photons and electrons generated by the initial interactions of primary photons. The kernel can be generated by measurement or by a modeling system such as Monte Carlo. A convolution-superposition employs a number of dose kernels that have been measured for various materials or modified for radiological path length using an electron-density specific scaling factor. A linear combination of each dose kernel convolution makes up the final result. Because the propagation of secondary photons and electrons is measured or modeled ahead of time, convolution and convolution-superposition algorithms are characteristically fast. [5, 19]

AAA

The anisotropic analytical algorithm, or AAA, is the convolution-superposition algorithm currently used at VIC for modeling most radiotherapy plans. It uses linear combinations of mono-energetic dose spread kernels, generated by EGSnrc Monte Carlo, to separately model lateral and depth scatter for primary photons, extra-focal photons and contaminant electrons before summing their contributions. Electron-density scaling factors are used to account for inhomogeneities in the lateral direction while a one-dimensional scatter kernel is employed along the depth axis to account for material interfaces. AAA has shown improved accuracy over its predecessors and good performance for most clinical applications. [15, 20]

2.2.2 Linear Boltzmann Transport Equation

The Linear Boltzmann Transport Equation is a differential equation or set of partial differential equations that govern the evolution of spatial and energy distributions of a population of particles [21]. For radiation therapy planning purposes the distribution of ionizing particles is of interest, so the LBTE takes the form of the partial differential equations

$$\hat{\Omega} \cdot \vec{\nabla}\Phi^{\gamma} + \sigma_t^{\gamma}\Phi^{\gamma} = q^{\gamma\gamma} + q^{e\gamma} + q^{\gamma}, \tag{2.4}$$

$$\hat{\Omega} \cdot \vec{\nabla}\Phi^{e} + \sigma_t^{e}\Phi^{e} - \frac{\partial}{\partial E}\left(S_R \Phi^{e}\right) = q^{ee} + q^{\gamma e} + q^{e}. \tag{2.5}$$

Equation 2.4 describes photon (γ) transport while equation 2.5 describes electron (e) transport. $\Phi^{\gamma}(\vec{r}, E, \hat{\Omega})$ and $\Phi^{e}(\vec{r}, E, \hat{\Omega})$ are the photon and electron angular fluence, respectively, $\vec{r}$ is a position vector, E is energy of the particle and $\hat{\Omega}$ is the unit direction vector. $\sigma_t^{\gamma}\left(\hat{r}, E\right)$ and $\sigma_t^{e}\left(\vec{r}, E\right)$ are total photon and electron cross sections, respectively, and $S_R\left(\vec{r}, E\right)$ is the restricted collisional and radiative stopping power, representing the continuous slowing down operator. The terms on the right hand side of equations (2.4) and (2.5) are primary and scatter source terms. q^{γ} and q^{e} are primary photon and electron source terms, respectively, $q^{\gamma\gamma}$ represents scattered photons due to photon interactions, q^{ee} represents scattered electrons due to electron interactions, $q^{e\gamma}$ represents scattered photons due to electron interactions and $q^{\gamma e}$

represents the reverse. [3]

Once Equations 2.4 and 2.5 are solved for electron fluence, the dose deposited at any given point can be found as the product of the local electron fluence and material specific stopping power:

$$D = \int_0^\infty \Phi^e S_R dE. \tag{2.6}$$

Monte Carlo provides a stochastic solution to the LBTE while Acuros XB solves these equations deterministically using an iterative approach. Both approaches are summarized below.

Monte Carlo

Monte Carlo simulations are stochastic solutions to the LBTE. A random number generator is used to sample the properties and interactions of single particles. These properties and interactions are stored in particle histories and accumulated over millions of particles to obtain a single solution; the more particles simulated, the less noise or variance present in the solution [5]. Particle interactions are modeled using fundamental physics principles and so, Monte Carlo solution accuracy is limited by the finite number of particles simulated and by uncertainty in user input rather than approximation of the physics [3].

The computation time required to simulate millions or billions of individual particles is appreciable: on the order of hours to days. For example, an open 18 MV field incident on an average patient sized phantom can take as long as 39 hours on a cluster of 36 1.8 GHz CPUs. To improve calculation efficiency, a number of standard approximations are made which contribute as little as possible to the overall systematic uncertainty. One such approximation is multiple scattering, a process by which many electron interactions, both elastic and inelastic, are treated as a single cumulative interaction or condensed history. This is done by sampling predetermined scatter or energy-loss distributions, and results in more efficient electron transport [22]. Other approximations vary by platform or by user preference and will be dealt with in Chapter 3.

Acuros External Beam

As outlined in the Thesis Scope, Acuros XB is a new commercial treatment planning product. The exact implementation of the algorithm is proprietary, but an overview of the approach is provided in a 2010 article by Vassiliev et al.

Acuros XB iteratively solves the form of the LBTE given in Equations (2.4) and (2.5) by discretizing in space, angle and energy. The calculation volume is turned into a discrete spatial grid with an adaptive mesh so that in regions of low dose-gradient, dose voxels may be larger and in regions of high dose-gradient, voxels are smaller for more calculation points. The change in voxel size is variable by factors of 2, so the next largest or next smallest voxel size is either twice or half the size of the current voxel. The multigroup method is used to divide photons and electrons into 25 and 49 energy groups, respectively, where each energy group is assigned a particular set of radiological properties. Angular discretization is performed using discrete ordinates which sets 32–512 weighted angles, depending on energy, for which the LBTE will hold [23]. The specifics of these discretizations are the crux to a deterministic solution of the LBTE free of significant systematic errors. Once electron fluence is solved for all points in the volume, Acuros XB uses stopping powers to calculate the dose delivered to each calculation point as in Equation (2.6). [3, 12, 13]

There is one modification to Equation (2.4) in the Acuros XB implementation, which is the omission of the second term on the right-hand-side of the equation, $q^{e\gamma}$. Rather than modeling photon production due to electron interactions, Acuros XB locally deposits all energy that is transfered from an electron to a photon. In addition, Equation (2.4) can be decoupled into three transport equations, one of which, Equation (2.7), handles only photons from the primary source or scattered in the treatment head, $\vec{\nabla}\Phi^{\gamma}_{unc}$, as

$$\hat{\Omega} \cdot \vec{\nabla}\Phi^{\gamma}_{unc} + \sigma^{\gamma}_{t}\Phi^{\gamma}_{unc} = q^{\gamma}(E, \hat{\Omega})\delta\left(\vec{r} - \vec{r_p}\right). \tag{2.7}$$

$q^{\gamma}(E, \hat{\Omega})$ is a photon point source located at $\vec{r_p}$ and solving this equation independently amounts to an initial ray-tracing activity. Once this is done, the transport equations are solved for electron fluence everywhere to determine dose as discussed above. [3]

2.3 Imaging and Contouring

Both medical images and radiation dose distributions are reported in a medical image format called DICOM. DICOM stands for *Digital Imaging and Communications in Medicine* and provides a standard format for the storage and transfer of clinical data such as diagnostic or planning images [24]. When dealing with image or dose files in this work, the files are in DICOM format.

2.3.1 Computed Tomography & Hounsfield Unit Saturation

Computed tomography, or CT, is the imaging modality used most often for radiation therapy treatment planning. An x-ray source mounted on a rotating gantry opposite a series of detectors moves around a patient taking a series of images at regular angular intervals. The attenuation of the x-ray beam measured at each angle is backprojected and processed to reproduce an attenuation map. As the patient is moved through the gantry, attenuation is measured along the length of the body, producing a 3D image. [24]

Each pixel of a CT image is represented by an integer called a Hounsfield Unit (HU). Hounsfield Units correspond to the linear attenuation of photons with an average energy of 75 keV by a material, compared to the attenuation of water [24]. For a voxel (x, y, z),

$$HU(x,y,z) = 1000\frac{\mu(x,y,z) - \mu_{water}}{\mu_{water}}. \tag{2.8}$$

Each CT imager has a fixed range of possible HU values and a unique linear piecewise conversion curve between HU and density, so a single treatment planning system may contain CT conversion data for multiple imagers. CT-saturation occurs when the imaging unit attempts to scan an object with density exceeding the scanner's range. These regions are assigned the highest available HU value, and so, density-specific information is lost. In addition, the presence of high density materials may result in total attenuation of the x-ray beam which is not processed normally by the backprojection algorithm and produces streaking, shadowing and blurring artifacts. In-house artifact suppression algorithms and complementary megavolt imaging have been explored as techniques for reducing high-density generated artifacts [25, 26]. Presently, however, these techniques are not widely used or easily integrated into the workflow of a busy clinic, and they are not immediately available at VIC.

2.3.2 Pixelation

Picture and volume elements, pixels and voxels, respectively, have a finite minimum size that determines the resolution of an image or dose distribution. This means that data that exist or events that occur over distances smaller than the pixel or voxel size may be lost through averaging necessitated by assigning one set of data to each image or dose element.

As well, depending on the display system interpreting the DICOM, the location of a pixel or voxel may be offset by up to a whole pixel or voxel width. For example, in a 2-D case, suppose one system interprets the image or dose information assigned to a pixel to correspond spatially to the top left corner of the pixel while another interprets the data to correspond to the center of the pixel. The result is two interpretations of the same data with a half pixel offset in the x- and y-directions as shown in Figure 2.3. Variations in spatial interpretation must be considered, along with volume averaging effects, when interpreting DICOM results.

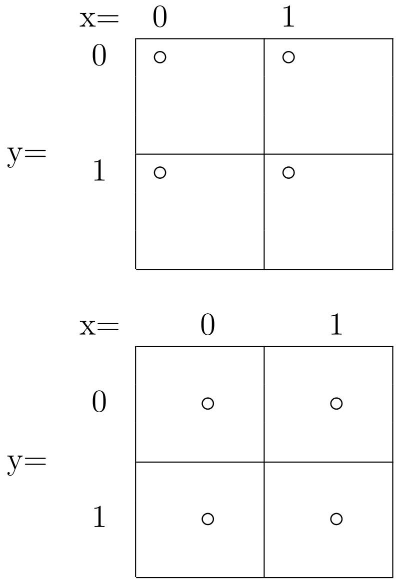

Figure 2.3: A single 2-D data set can be interpreted in a number of ways. Top: Spatial information is assigned to the top left corner of the pixel. Bottom: Spatial information is assigned to the centre of the pixel.

2.3.3 Contouring

In planning radiation therapy treatments, dosimetrists, oncologists and physicists evaluate the dose delivered to specific volumes such as the tumour mass and critical organs. To facilitate this, treatment planning systems provide tools to delineate each of these volumes with a structure called a contour. Contours can be either hand drawn or automatically created by the treatment planning system, and are not only useful for evaluation purposes, but also for optimization algorithms where a conformal dose to some volume can be weighted against the sparing of another. In the case of erroneous HU assignment, contouring can be used to reassign appropriate material properties, including properties for materials beyond the HU range of the CT scanner. This is a useful tool when assigning material properties to high-density implants, but CT saturation is usually accompanied by an increase in image artifacts, as well as blurring of the object's dimensions, which are not as easily corrected.

Contouring has some important limitations, the foremost being the pixelation effects discussed in the previous section. In addition, some treatment planning systems, such as Eclipse, use vector based contours and there is uncertainty as to how pixels along the contour-boundary are assigned. In this research it has been observed that vector contours are not ideal for handling sharp angles and that synthetic volumes with sharp angles are not contoured accurately. Overall, it should be emphasized that contours are virtual structures superimposed onto CT density maps as tools with associated uncertainties.

2.4 Radio-chromic Film

A set of experimental measurements to be introduced in Chapter 3 were performed using radio-chromic film, a radiation-sensitive film used in relative dosimetry. Its properties are closer to tissue than silver-based films, and unlike the dedicated wet labs required for chemical processing of silver-based films, radio-chromic film is self-developing. In addition, radio-chromic film is insensitive to visible light, making it easy to handle. Because of these advantages and its continuing improvements in performance, radio-chromic film is gradually replacing silver-based film in dosimetric and diagnostic applications.

Generally, radio-chromic film consists of an active layer of photomonomer molecules mounted on a polyester base. When exposed to radiation, the photomonomer molecules are excited by photons, electrons, or other energetic molecules, and this produces a chemical change resulting in a colour change. The film requires only a few milliseconds to develop, but may require up to an hour to become chemically stable, so reading usually takes place after some time period as recommended by the manufacturer. [27]

As a relative dosimeter, radio-chromic film must be calibrated before it can be used for measurements. This can be done by delivering a known range of doses to film from the batch to be used in the measurements, taking care to keep a sample unirradiated for a 0 Gy fog and base reading. These calibration measurements can be used to create an optical density (OD) to dose conversion curve. Optical density is a measure of light transmission and is given by

$$OD = \log_{10}\left(\frac{I_0}{I}\right) \tag{2.9}$$

where I_0 is the initial light intensity and I is the transmitted light intensity. A densitometer is used to measure OD by directly measuring transmitted light through a sample and comparing with the known intensity of the light source. Because radio-chromic film has some directional dependance, film orientation should be noted and consistent through the calibration, measurement and readout process. Once the calibration curve is established, additional films can be irradiated and their measured OD converted to dose. [24]

2.5 Summary

Chapter 2 has covered photon and electron interactions at therapeutic energies, radiotherapy modeling techniques, CT imaging and processing for radiotherapy planning, and the properties and use of radio-chromic film for relative dosimetry. In Chapter 3, these ideas are applied to experimental measurements and calculations to enable an evaluation of Acuros XB as applied to radiotherapy planning around high-density implants.

Chapter 3

Methods & Materials

In order to evaluate Acuros XB for dose calculations involving high-density perturbations using Monte Carlo as the reference, the parameters of the dose calculation algorithms must be understood and matched as closely as possible. Chapter 3 summarizes the modeling parameters used and approximations made by Acuros XB, EGSnrc Monte Carlo and AAA. The experimental measurements and calculations performed are also outlined, as well as some of the evaluation techniques used to analyze the results.

3.1 Modeling Environments & Parameters

3.1.1 Introduction

Monte Carlo

All of the Monte Carlo modeling in this work was done using BEAMnrc and DOSXYZnrc which are built on the EGSnrc code system [28]. BEAMnrc models beam production, shaping and transport through the linear accelerator while DOSXYZnrc transports the resulting particle histories through a patient or phantom geometry in order to score dose deposition [29, 30]. The patient or phantom geometry is generated by a program called *ctcreate* which reads a set of CT DICOM files and converts the data into a file containing spatial, material and density information that is useable by the EGSnrc system. The conversion from HU to material and density values is user defined and will be discussed further in Section 3.1.3. Thirty-six 1.8 GHz CPUs housed in three computer nodes comprise the Beowulf cluster that runs Monte Carlo calculations at VIC. The cluster was set up and is run on a front end node by Rocks Cluster Distribution from National Partnership for Advanced Computational Infrastructure while the workload is managed by Condor. User input is done through a web-based application networked through the front end node.

The BEAMnrc and DOSXYZnrc code systems are widely used and trusted for benchmarking, and the VIC implementation is no exception [3, 13, 14, 15, 31]. For this reason, Monte Carlo solutions will be used as the reference in calculation comparisons throughout this work.

Eclipse

Eclipse is the commercial treatment planning software package distributed by Varian Medical Systems that is used at VIC and in this work. Eclipse provides a single user interface for a number of calculation algorithms including pencil beam convolutions, AAA and most recently, Acuros XB. The system provides a graphical user interface for contouring structures and planning treatment fields on a 3D planning image, usually a CT DICOM set. As well, the program provides an environment for comparing plans and dose distributions. Some Eclipse features are shared between AAA and Acuros XB while others are specific to each algorithm. In the following discussion of modeling parameters, when a feature applies to both algorithms it will be discussed under the heading Eclipse, otherwise, it will be discussed under the headings AAA and Acuros XB.

3.1.2 Source Model

Monte Carlo

The radiation source model generated by BEAMnrc has been tuned to match the output of the Varian Clinac® 21EX linear accelerators used for radiation therapy treatment at VIC. Electrons and photons are transported through the explicitly modeled internal structure of the linear accelerator head to produce a phase space that defines the position, direction, energy and charge information of each photon or electron that crosses a particular spatial plane of the model. At VIC, output models have been created for 18 and 6 MV spectral photons, both of which are used in the experimental calculations to follow.

Eclipse

Eclipse provides the same radiation source model for Acuros XB and AAA calculations. The source model has also been tuned to match the output of a Varian Clinac 21EX linear accelerator using a proprietary configuration algorithm that modifies parameter values until the modeled output matches set of beam measurements provided by the user, including profiles and depth doses for various field sizes. Again, output models have been configured for 18 and 6 MV spectral photon beams.

3.1.3 Material Data

For EGSnrc Monte Carlo and Eclipse, material and density assignment is performed according to a user defined HU to density conversion curve which is specific to the CT imager used to acquire the planning image. For this research, the curves had to be artificially extended to include titanium alloy and stainless steel by adding points to the conversion curve beyond 4000 HU and 4.0 g/cm^3. The resulting conversion curves are shown in Figure 3.1 and the properties of stainless steel and titanium alloy are compared to those of muscle in Table 3.1. Co-Cr-Mo alloy is a common prosthesis material that is considered in the literature, but has been left out of the Eclipse materials list [11]. The properties of Co-Cr-Mo are so close to those of stainless steel, however, that there should be very little qualitative difference between dose distributions calculated for either material. For completeness, and to facilitate discussion in Section 3.2 the properties of Co-Cr-Mo are included in Table 3.1.

Monte Carlo

Material cross section data used for EGSnrc Monte Carlo calculations are generated by the program PEGS4 contained in the EGSnrc code system package. PEGS4 uses material composition input data (Table A.1) to create cross section libraries that are referenced by BEAMnrc and DOSXYZnrc. For efficiency purposes, EGSnrc limits the number of materials that may be assigned to any one calculation volume. The materials available to EGSnrc Monte Carlo in this work and their density ranges are presented in Table 3.2.

Table 3.1: Material properties for muscle, titanium, stainless steel and Co-Cr-Mo [8, 11].

Material	Muscle	Titanium	Stainless Steel	Co-Cr-Mo
Mass Density (g/cm^3)	1.04	4.3	8.1	7.9
Electron Density (e^-/cm^3)	3.4×10^{23}	1.2×10^{24}	2.3×10^{24}	2.2×10^{24}
Effective Atomic Number	7.64	21.4	26.7	27.6

Eclipse

As mentioned earlier, the HU to density conversions shown in Figure 3.1 are defined by the user. However, the allowed density range for each material is fixed by Eclipse. In the context of this work, this meant only that the Monte Carlo conversion curve was modified to match that of Eclipse, and not the other way around.

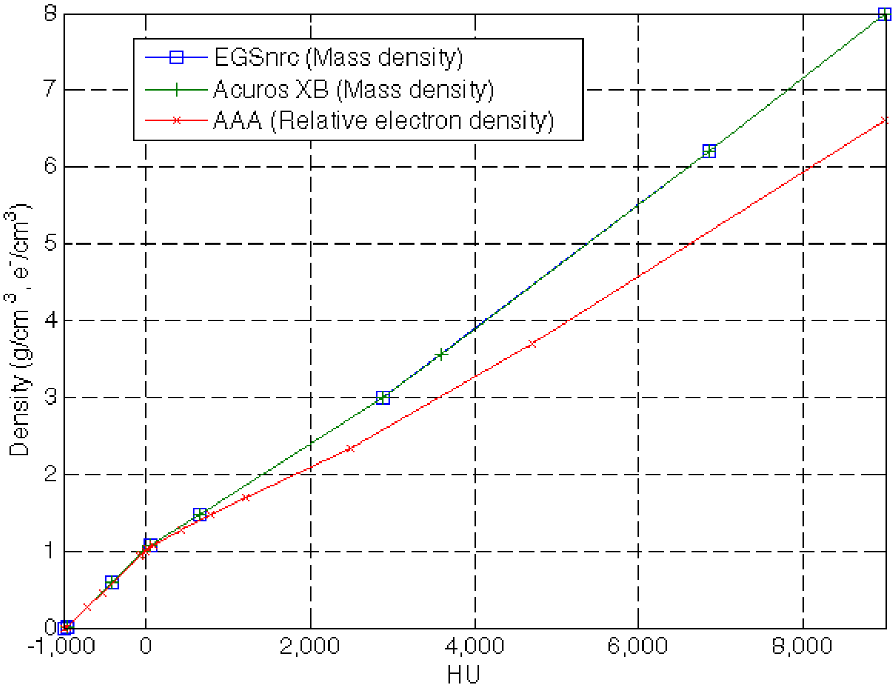

Figure 3.1: HU to mass- and electron-density conversion curves for Eclipse and EGSnrc Monte Carlo.

Acuros XB includes an important high-density material assignment restriction: any voxel containing an HU value that corresponds to a density greater than 3.0 g/cm^3 must be included in a structure and assigned a specific material or the calculation will be prevented from proceeding. The partial inclusion of high density voxels by vector-based contours means that contours defining high-density structures often require an external margin of 0.1 cm, as recommended by Varian, to encompass the entire object. This artificially inflates the size of the structure, but is necessary to proceed with the calculation.

Table 3.2: Materials and corresponding density ranges for Eclipse and EGSnrc Monte Carlo.

Eclipse			Monte Carlo		
Material	Min ρ	Max ρ	Material	Min ρ	Max ρ
	(g/cm^3)			(g/cm^3)	
Air	0.0010	0.0112	Air	0.0	0.0114
Lung	0.0010	0.5896	Lung	0.0114	0.5896
Adipose	0.5907	0.9849	Muscle	0.5896	1.0748
Muscle	0.9853	1.0748			
Cartilage	1.0758	1.4749	Light Bone	1.0748	1.4749
Bone	1.4755	2.9997	Bone	1.4749	2.9997
Aluminum	2.2754	3.5600			
Titanium Alloy	3.5600	6.2096	Titanium Alloy	2.9997	6.2096
Stainless Steel	6.2104	8.0	Stainless Steel	6.2096	8.0

3.1.4 Interactions & Approximations

Monte Carlo

In VIC's implementation of the code, EGSnrc models the photoelectric effect, Compton scattering, pair-production, positron annihilation and bremsstrahlung radiation. It takes relativistic spin effects into account for electron transport and multiple scattering is used for more efficient charged particle propagation [22]. For efficiency, Rayleigh scattering is not modeled and characteristic x-rays are handled only approximately: for a photoelectric interaction, the energy that would be lost to overcome binding energy and then emitted during atomic relaxation is transferred entirely to the photoelectron. Bethe-Heitler cross-sections are used for bremsstrahlung radiation, the Klein-Nishina formula determines Compton scattering cross-sections and photoelectrons inherit the direction of incident photons. [29]

The parameter ECUT, electron cutoff energy, defines the energy at which it is assumed that an electron will not be capable of leaving the current voxel and its remaining energy deposited locally. The default value of ECUT is 0.7 MeV for a remainder electron energy of 0.189 MeV after subtracting the electron rest mass, 0.511 MeV. To be sure that this parameter was appropriate for high density-gradient scenarios, calculations were performed using an ECUT value of 0.521 MeV for a minimum electron energy of 0.010 MeV. Differences between the results were not statistically significant, and the lower ECUT value almost doubled calculation time, so ECUT = 0.7 MeV was used. [29]

Acuros XB

As discussed in Chapter 2, Acuros XB uses ray tracing to transport primary and scattered source photons to the calculation volume, while charged particles are propagated by solving Equations (2.4) and (2.5) with some physical approximations, listed here. Both secondary charged particles produced in pair production are modeled as electrons instead of one electron and one positron, and, as mentioned before, photons produced by electrons are not modeled explicitly. Instead, energy from bremsstrahlung radiation and characteristic x-rays is deposited locally.

AAA

Chapter 2 discusses how AAA uses dose kernels and electron-density scaling to simulate dose scattered laterally from a ray of photons, and one-dimensional dose kernels to deal with inhomogeneities with depth. As the dose kernels are generated using EGSnrc Monte Carlo, AAA effectively models all of the interactions that EGSnrc Monte Carlo models. However, the pre-calculated kernels are calculated for water and scaled depending on the material of interest in the calculation volume. This technique is insufficient when dealing with sharp dose perturbations due to a high-density object . Consequently, throughout the experimental cases presented in the following chapters AAA is not expected to accurately handle high-density dose perturbations. This is not meant to discredit AAA as a clinically useful algorithm, only to highlight its limitations for one subset of clinical applications.

3.2 Experimental Measurements

As discussed in Chapter 2, the presence of a high-density object in a radiation field is expected to increase secondary photon and electron scattering, resulting in elevated dose at the entrance and lateral surfaces of the object while shadowing regions beyond it. These perturbations are presented in Figure 1.5, which shows dose profile and depth dose plots of EGSnrc Monte Carlo data for 18 MV photons through a phantom with and without a high-density centre. A variation on this data was presented in a 2003 Task Group Report of the American Association of Physicists in Medicine (AAPM) that encompassed recommendations for treatment planning for patients with hip prostheses. The Monte Carlo data presented in this document, generated by an unspecified Monte Carlo system, has been reproduced with permission in Figure 3.2 and shows a 30% dose peak at the distal surface of a Co-Cr-Mo centre, allegedly due to pair-production interactions within the metal [11]. This forward peak was not seen in the EGSnrc Monte Carlo data used in this work, nor in Acuros XB results. Consequently, a set of film measurements were performed to ascertain which model is closest to reality.

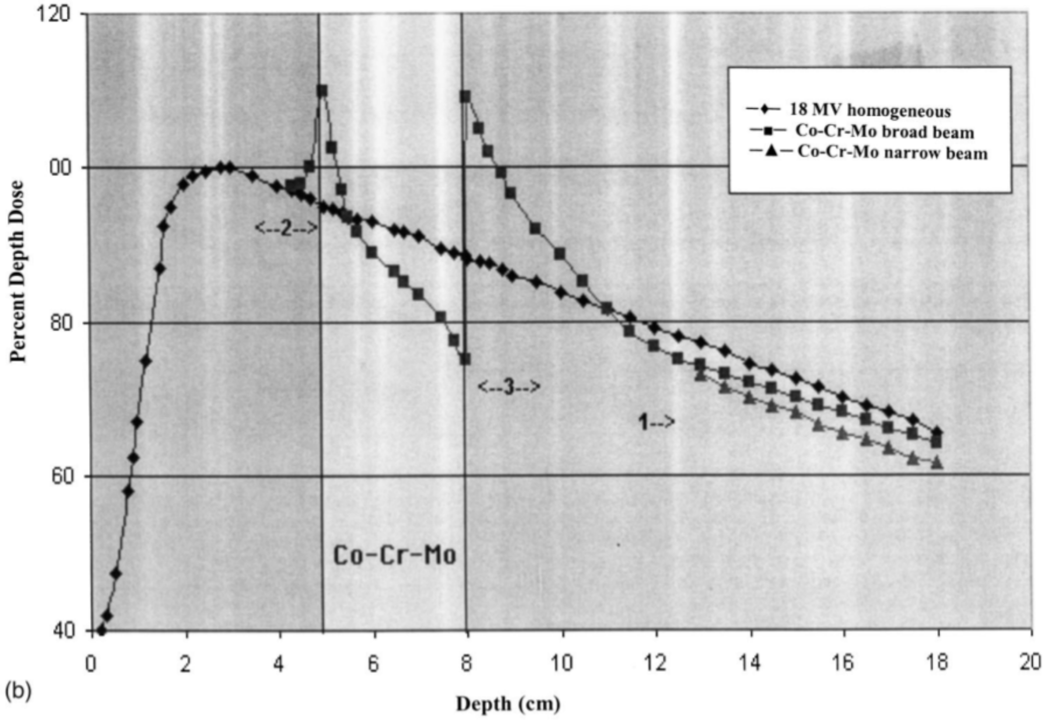

Figure 3.2: Depth dose perturbation data included in AAPM TG Report 63 [11]. Reproduced with permission from the AAPM.

Although the data presented in the Task Group Report was for 18 MV photons through a Co-Cr-Mo slab, the measurements presented here were performed using 18 MV photons through a slab of steel with the same dimensions. The properties of steel are close enough to Co-Cr-Mo that there should be no qualitative difference in the dose distribution. The steel slab was placed between slabs of Solid Water® with sections of Gafchromic® EBT2 radio-chromic film placed at intervals throughout. Figure 3.3 shows the geometric setup used for the measurements. Arranging the stack with the upper steel surface at isocenter, labeled with a red x, 5 cm Solid Water was placed on top of the steel with film placed at 3.5 cm (d_{max}), 4.5 cm and 5.0 cm depth. The 3.0 cm deep steel, in turn, was placed on a 10 cm stack of Solid Water with film placed at 8.0 cm, 8.5 cm, 9.0 cm and 10.0 cm depths.

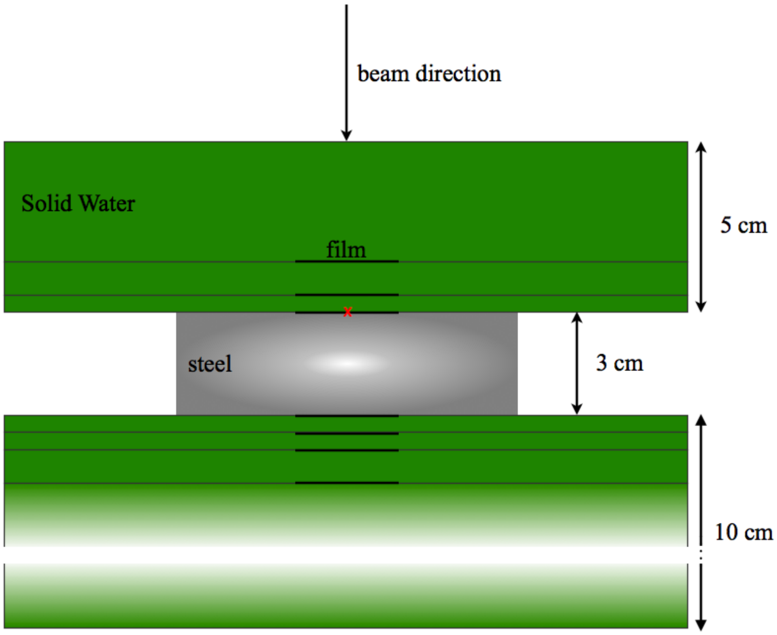

Figure 3.3: Illustration of the experimental setup used to measure high-density forward scatter due to a 10x10 cm^2 field of 18 MV photons through steel. The red x marks isocentre and sections of film are placed at 3.5, 4.5, 5,0, 8.0, 8.5, 9.0 and 10.0 cm depths (from top, down).

The steel, Solid Water and film were stacked on the couch of a Varian Clinac 21EX linear accelerator and centered in a 10x10 cm^2 field. After acquiring a set of calibration films at 0, 100, 200 and 300 cGy, 250 monitor units (MU) were delivered using 18 MV photons at 95.0 cm from source to surface (SSD) and 100.0 cm from

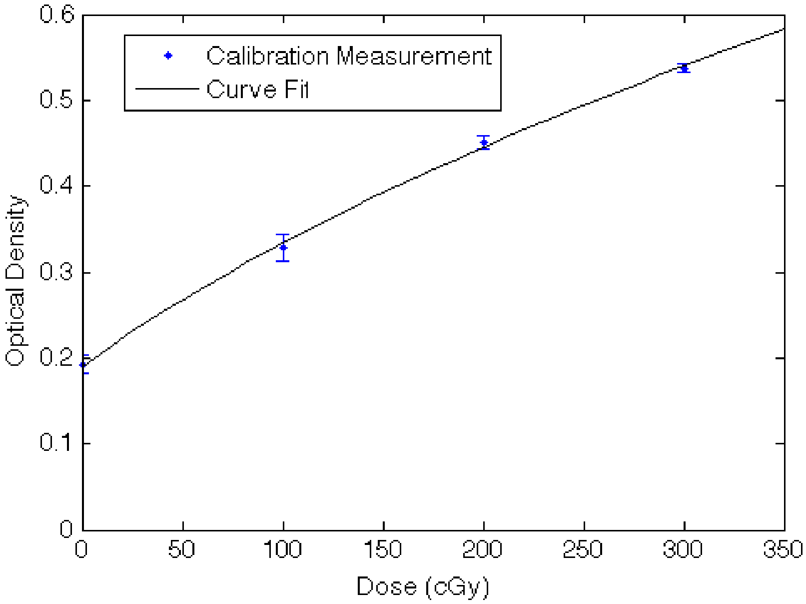

Figure 3.4: Calibration curve for Gafchromic® EBT2 radio-chromic dosimetric film.

source to the isocentre (SAD). The film was placed in an envelope and allowed to stabilize before a MacBeth Process Measurements TD932 Densitometer was used to measure the OD of each film. Eight measurements of OD were taken for each film and used to calculated a mean value and standard deviation. The calibration curve, fitted with a square root function, is shown in Figure 3.4. Error bars on each data point are representative of the standard deviation of measured values.

A virtual phantom of the experimental setup was generated in Eclipse by creating structures in an empty CT image and assigning appropriate material and density properties. The Solid Water regions were assigned skeletal muscle with 0 HU contents corresponding to 1.0 g/cm^3 while steel was assigned stainless steel with 8999 HU corresponding to 8.0 g/cm^3. Acuros XB, AAA and EGSnrc Monte Carlo were then used to calculate the depth doses expected from the film measurements. Acuros XB and AAA data were calculated on a 0.1 cm voxel grid while EGSnrc Monte Carlo data was calculated on a 0.2 cm voxel grid as 0.2 cm was the finest resolution available for the size of CT image used.

3.3 Experimental Calculations

The primary method used for evaluating the accuracy of Acuros XB is comparison with EGSnrc Monte Carlo simulations for a number of phantom geometries of varying complexity. The evaluation starts with a high-density rectangular rod inside a skeletal muscle cube, continues with a water tank containing high-density cylindrical rods and prostheses, and concludes with a patient CT and clinical treatment plan. Monte Carlo simulations were performed to 1-2% standard deviation: approximately 7×10^9 particles and 5×10^9 particles for 18 MV and 6 MV fields respectively, except for the clinical case where 3.5×10^9 particles were simulated.

3.3.1 Virtual Phantoms

In order to reduce potential sources of variation, initial experimental calculations were performed for virtual phantoms with regular geometries and sharp boundaries. To construct these phantoms, empty CT DICOM image sets were modified using Mathworks® MATLAB®, Natick, MA, USA, and imported into Eclipse. The re-

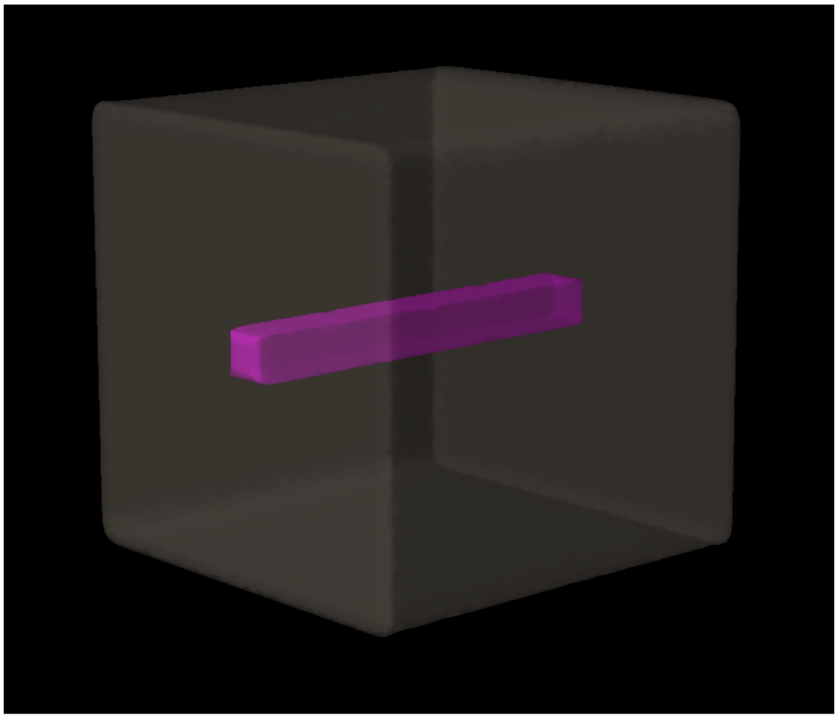

Figure 3.5: A 20x20x20 cm^3 virtual skeletal muscle phantom containing a stainless steel rod centre.

sulting virtual phantoms are 20x20x20 cm^3 and 10x10x10 cm^3 skeletal muscle cubes, each containing a stainless steel rod with a 2x2 cm^2 square cross-section at its center, oriented to be longest in the z-direction. Each slice has a resolution of 0.05 cm in the x- and y-directions with slice thickness of 0.5 cm. A 3-D rendering of the larger phantom is shown in Figure 3.5.

The high-density rod must be contoured and assigned a material in order for Acuros XB to run, so it was possible to use the same phantoms for stainless steel, titanium alloy and skeletal muscle internal structures by changing the material properties of the rod structure. Plans for these phantoms involved 10x10 cm^2 and 5x5 cm^2 fields focused on isocenter, both on-axis and at a 10° gantry angle using 18 and 6 MV photons.

3.3.2 Water Tank Phantoms

A water tank containing high density objects was scanned using a clinical CT unit and loaded into Eclipse for planning and dose modeling. The water tank itself is 30x30x30 cm^3 and is shown in Figure 3.8. For the scan, the tank was supported on 5 cm of Solid Water. Two plastic positioning guides were placed on the bottom of the tank for reproducible setup and the tank was filled with water to the top of the blue insert that can be seen at the top of Figure 3.8. A foam block, which is not shown in the figure, was placed on top of the water to minimize motion during the CT scan.

Figure 3.6: Top: Stainless steel rod. Bottom left: Steel alloy hip prosthesis. Bottom right: Titanium alloy hip prosthesis.

Stainless Steel Rods

The first water tank geometry consists of two cylindrical stainless steel rods 20.32 cm (8 in) long and 2.54 cm (1 in) in diameter, shown in Figure 3.6 (top). The rods were oriented on an angle of 10° and centered about 3.65 cm on either side of the central beam axis. For calculation purposes, these rods were contoured as stainless steel and subject to 10x10 cm^2 fields of 18 MV and 6 MV photons delivered on axis. The Eclipse-generated structure set for this phantom is shown in Figure 3.7.

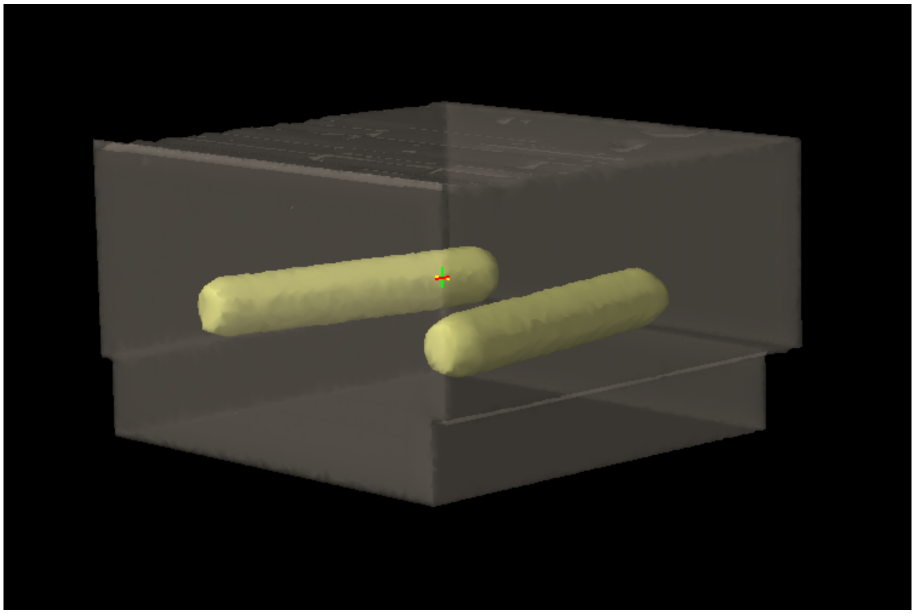

Figure 3.7: Eclipse generated structure set for a plexiglass water tank containing cylindrical stainless steel rods.

Hip Prostheses

The second water tank geometry includes two hip prostheses, one a steel alloy and the other a titanium alloy, both shown in Figure 3.6 (bottom). The exact properties of the pieces are unknown, however, because their geometries are used only for computational purposes, throughout this work they are assumed to be solid. For calculations, the prostheses are contoured as stainless steel and titanium alloy, respectively, and subject to 10x10 cm^2 fields of 18 MV and 6 MV photons. The Eclipse generated structure set for this phantom geometry is shown in the bottom image of Figure 3.8.

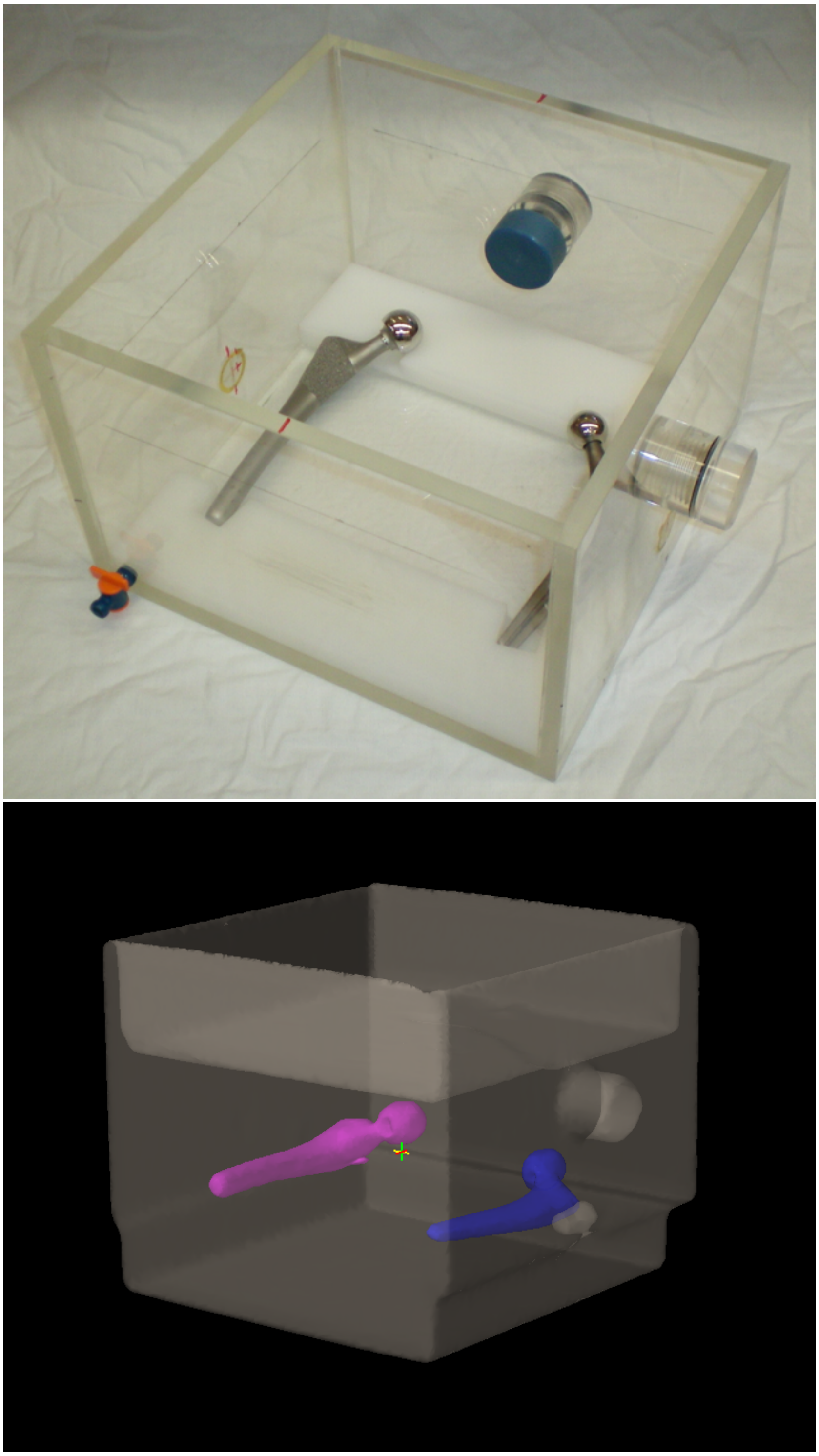

Figure 3.8: Top: Water tank used for imaging steel rods and hip prostheses. The hip prostheses are shown in the positioning guides while the foam block is not shown. Bottom: Eclipse generated structure set for the plexiglass water tank containing the hip prostheses.

3.3.3 Clinical Patient Data Set

The final geometry examined in this work is an anonymized clinical patient CT along with the prostate treatment plan that was initially modeled using AAA and delivered at VIC. A contoured axial slice of the patient CT is shown in Figure 3.9. The patient has a unilateral, left hip prosthesis which has been outlined in pink, assigned the properties of stainless steel and rendered white on each slice of the contoured CT. The clinical target volume is outlined in blue, the planning target volume, which accounts for variations in daily set-up, in red, the right femur in green and the rectum is the lowest contoured region outlined in faded red. The treatment plan is a standard conformal five-field approach that uses beam modifiers to obtain a homogeneous dose in the target volume, but that has been adjusted to avoid treating through the prosthetic hip.

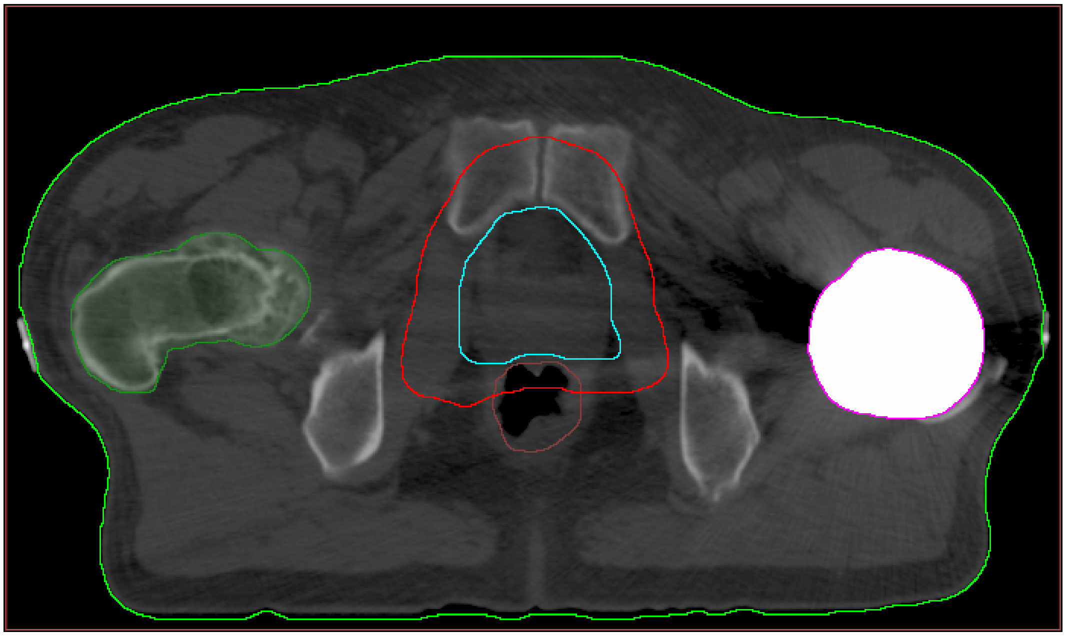

Figure 3.9: Contoured planning CT for an anonymized prostate patient with a unilateral hip prosthesis.

3.4 Reporting Methods

3.4.1 Profile & Depth Doses

In the presentation of data in Chapter 4 the terms *dose profile* and *depth dose* will be used to describe plots. In all cases, a dose profile will refer to an array of data points taken laterally from a single axial slice, perpendicular to the beam axis. Depth dose will refer to an array of data points taken from a single axial slice in the direction of the beam axis.

3.4.2 γ Evaluations

When dealing with large data sets involving high dose- and density-gradients within complex geometries, such as human anatomy, it is usually impractical to compare dose calculations voxel to voxel. A distribution with steep dose gradient and a single voxel offset everywhere may represent the same dose deposition as a reference distribution, but be evaluated as incorrect because of the offset. To address this, the concept of distance to agreement has been integrated with percent dose difference to produce the γ index, a radial measurement of the distance between agreeing dose points in two distributions [32]. For a reference dose, D_{ref}, at position r_{ref} and corresponding analysis dose, D_c, at position r_c, if the dose-difference and distance to agreement criterion are ΔD_M and Δd_M, respectively, the gamma index is defined as

$$\gamma(r_{ref}) = min\left\{\sqrt{\frac{r^2}{\Delta d_M^2} + \frac{\delta^2}{\Delta D_M^2}}\right\} \forall\{r_c\} \tag{3.1}$$

where

$$r = |r_c - r_{ref}|, \tag{3.2}$$

$$\delta = D_c(r_c) - D_{ref}(r_{ref}). \tag{3.3}$$

If $\gamma \leq 1$ then the evaluation passes, otherwise, if $\gamma > 1$ the evaluation fails. The advantage of a γ-analysis over a point by point comparison is the allowance for spatial or dose variations that result from averaging due to pixelation, variation in contour interpretation and the presence of high dose- or density-gradients. In Chapter 4, γ-evaluations will be performed to evaluate Acuros XB and AAA data against EGSnrc Monte Carlo results for each of the calculations described in this chapter. Each 3D matrix of γ-values will be reported as a percentage of voxels with $\gamma \leq 1$, or within tolerance.

Chapter 4

Results

Chapter 3 outlined experimental calculations performed for real and virtual phantoms, a prostate treatment plan for a patient with a unilateral hip prosthesis, and film measurements undertaken to evaluate the distribution of dose on the distal interface of a high-density region with Solid Water. The results of these calculations and measurements are presented in the following chapter, beginning with film measurement results. These are followed by a summary of the phantom and patient calculations and a brief description of algorithm calculation times.

4.1 Film Measurements

Figure 4.1 presents the results of the film measurements described in Section 3.2. Each data point represents the mean of eight OD measurements and the error-bars represent the corresponding standard deviations. EGSnrc Monte Carlo, Acuros XB and AAA were used to calculate the expected dose and are compared to the film measurement data. The shape of the Monte Carlo depth dose data included in the AAPM Task Group Report on planning for patients with hip prostheses, Figure 3.2, suggests that there should be a forward scatter peak in excess of 30% on the distal surface of the high-density inhomogeneity, however, neither the measured data, nor the modeled data produces such a peak. Both Acuros XB and Monte Carlo outline a build-up peak on the distal surface of the inhomogeneity due to reestablishment of electron equilibrium, but this peak is on the order of 5%, much less than the 30% peak presented in Figure 3.2. The film measurements confirm the absence of a dramatic forward peak and reaffirm the validity of the data to be presented in the remainder of this chapter, which are void of such a peak. [11]

The percent differences between measured and calculated data are also presented in Figure 4.1. The large differences at 5.0 and 8.0 cm depths are likely due to uncertainties in high-density boundary definition.

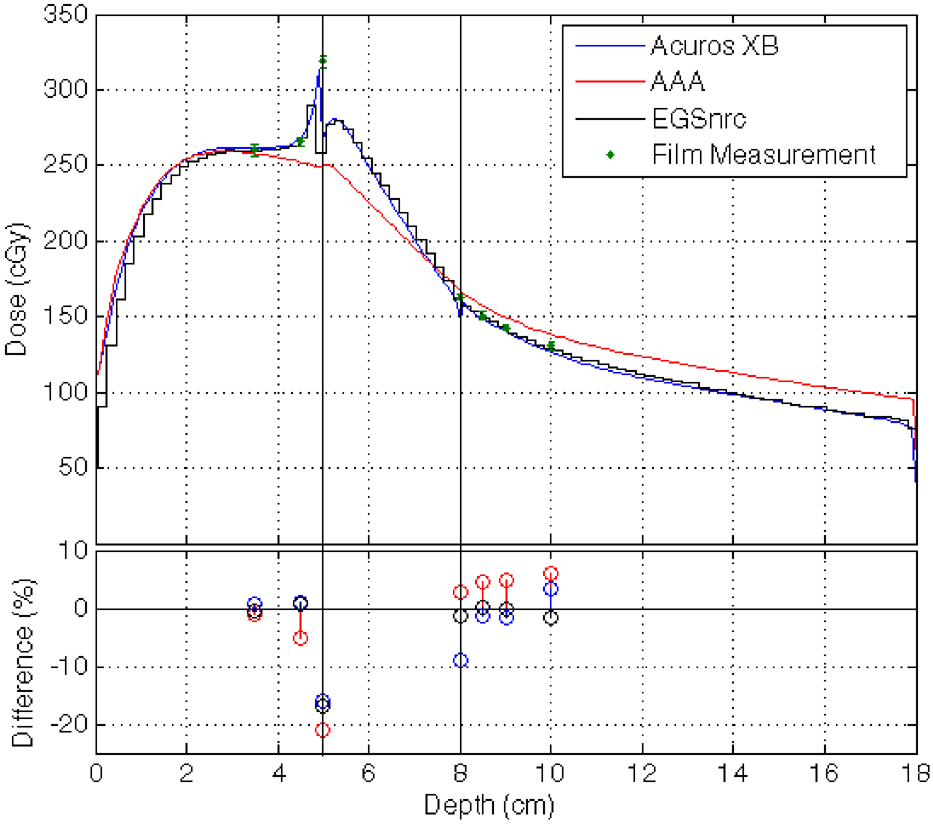

Figure 4.1: Film measurements and Acuros XB, AAA and EGSnrc Monte Carlo data for a 10x10 cm^2 field of 18 MV photons through the high-density inhomogeneity outlined in Figure 3.2. Percent differences between measured and calculated results are plotted in the lower portion of the graph. The solid black lines at 5 and 8 cm depth indicate the steel boundaries.

4.2 Virtual Phantoms

20x20x20 cm^3 Cubic Phantom

Figure 4.2 shows depth dose plots for a 10x10 cm^2 field of 18 MV photons delivered normal to the surface of the 20x20x20 cm^3 virtual phantom described in Section 3.3.1 as calculated by Acuros XB, AAA and Monte Carlo. The dose grid has a resolution of 0.2 cm in all directions and the data has been normalized to 100% at 5 cm depth along the beam axis. Label (i) in the figure shows the approximately 15% backscatter peak that results from the increase of secondary electrons being scattered backwards

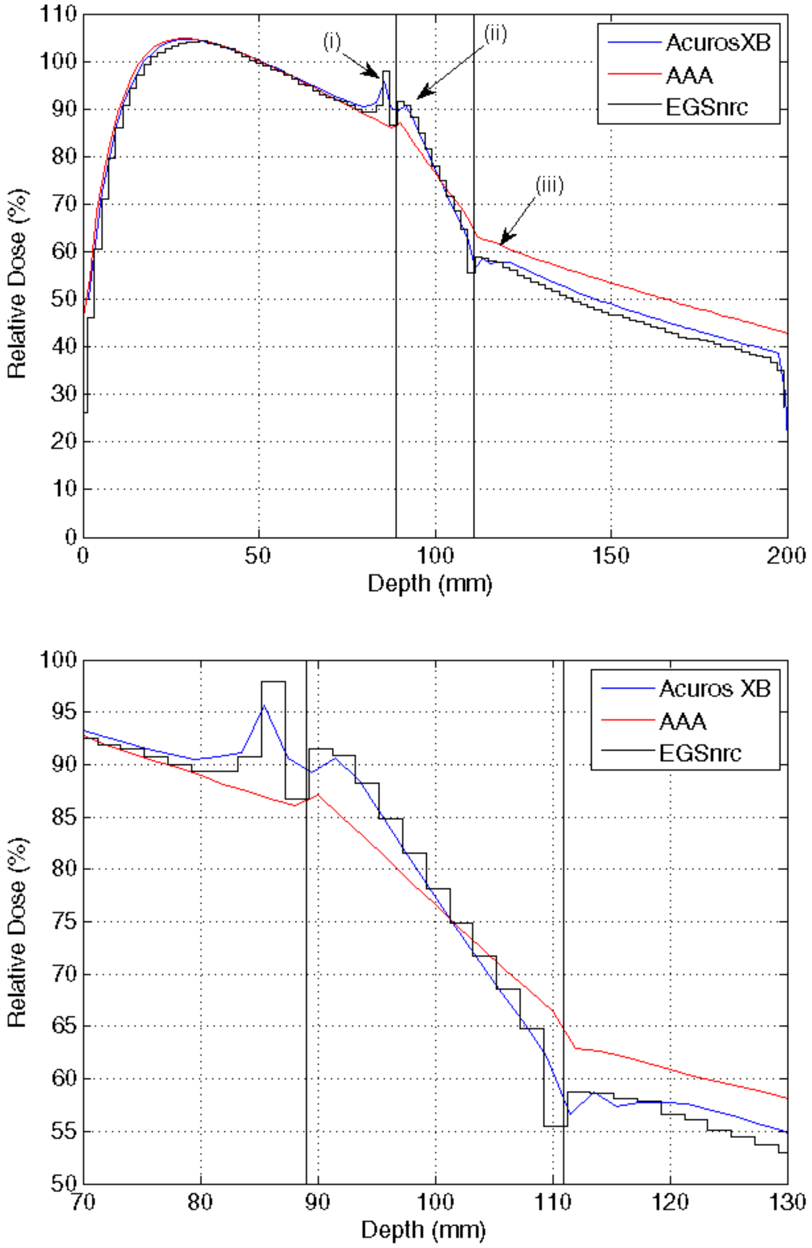

Figure 4.2: Depth dose plot for 18 MV photons through a skeletal muscle cube with a stainless steel centre (magnified on bottom). The vertical black lines indicate the high-density boundaries. (i) Backscatter peak. (ii) High-density electron equilibrium build up. (iii) Exit dose drop and skeletal muscle electron equilibrium build up.

with a range of 10–12 mm beyond the high-density region. Next, the build-up region inside the high-density volume is labeled (ii) and is due to the establishment of a new electron equilibrium within the metal. Finally, at the far end of the metal volume, label (iii), dose builds down and then back up on either side of the interface. This electron disequilibrium effect is expected: the build-down occurs due to the reduction of electrons scattered backwards from tissue compared to stainless steel and the buld-up, again, occurs as electron equilibrium is reestablished. These features are shown in greater detail in the bottom panel.

Considering positional uncertainties and statistical variations, the Acuros XB data agrees very well with the Monte Carlo data. In particular, Acuros XB shows the ability to model the high-density backscattered dose that AAA's empirical depth scatter kernel is unable to handle. AAA shows a small peak just inside the stainless steel, but it lies between the expected positions of the backscatter and build-up peaks and its height is far less than the height of either peak as modeled by Acuros XB or Monte Carlo. The beam attenuation by the stainless steel volume is matched very closely between Acuros XB and Monte Carlo while there is about a 5% overestimate of the corresponding dose as calculated by AAA.

Figure 4.3 shows a dose profile corresponding to the depth dose discussed above. Taken at y=10.05 cm depth, these profiles clearly display the difference in modeling of lateral scatter by Acuros XB and Monte Carlo compared to AAA. Acuros XB and Monte Carlo data show approximately 15% peaks that are well within positional and statistical uncertainties of each other and extend 15–16 mm from the metal's lateral surface. The difference in dose between the Boltzmann solvers and AAA is striking, reaching as much as 10% near the lateral surfaces. AAA's lateral scattering kernel and electron-density scaling corrections reach a solution that is very different from that produced by Acuros XB and Monte Carlo.

Figures 4.4 – 4.10 show variations on the scenario presented in Figure 4.2. The profile and depth dose in Figures 4.4 and 4.5 result from a 6 MV photon beam incident on the same skeletal muscle phantom and stainless steel inhomogeneity. Those in Figure 4.6 are due to an 18 MV beam delivered with a 10° gantry angle. The profile and depth dose in Figures 4.7 and 4.8 are calculated for 18 MV photons delivered without a gantry rotation to the same skeletal muscle phantom, but with a titanium alloy inhomogeneity, while Figures 4.9 and 4.10 show data for the same titanium alloy volume, but for a 6 MV beam. The 18 MV cases were normalized, again, to 100% at 5 cm depth along the normal beam axis while the 6 MV cases were normalized to

100% at 3 cm depth along the beam axis. All of the dose data were calculated at a resolution of 0.2 cm in all directions and γ-analyses were performed at 2% and 2 mm for voxels containing at least half the maximum dose for each data set. The results are summarized in Table 4.1.

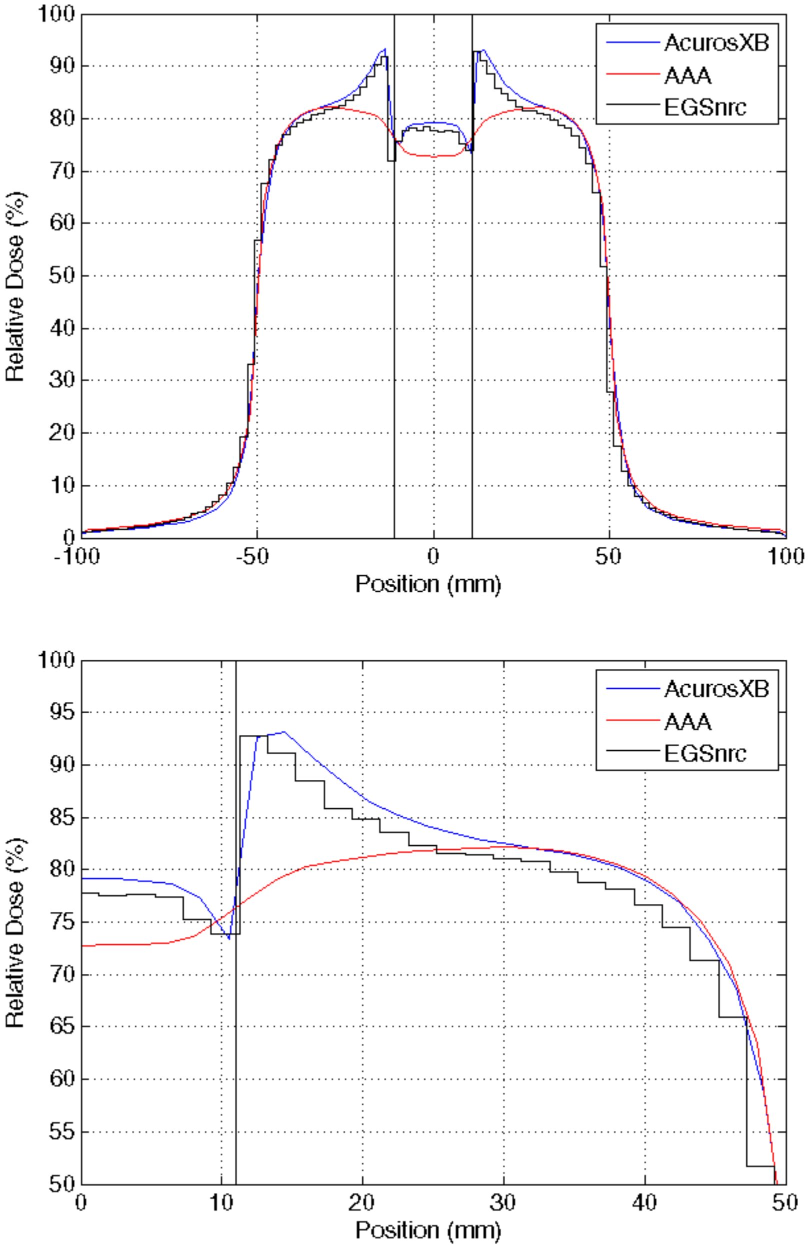

Figure 4.3: Dose profile plot for 18 MV photons through a skeletal muscle cube with a stainless steel centre (magnified on bottom). The vertical black lines indicate the high-density boundaries.

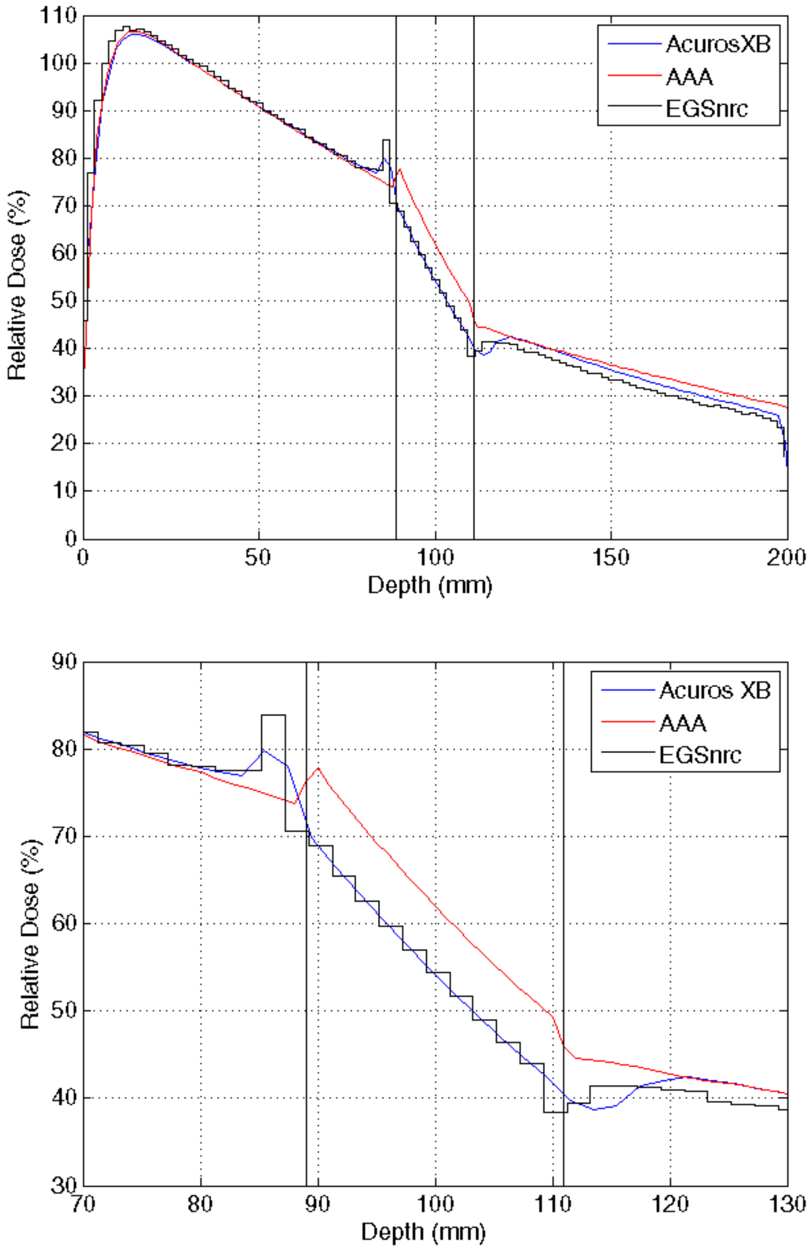

Figure 4.4: Depth dose plot for 6 MV photons through a 20x20x20 cm^3 skeletal muscle cube with a stainless steel centre (magnified on bottom). The vertical black lines indicate the high-density boundaries.

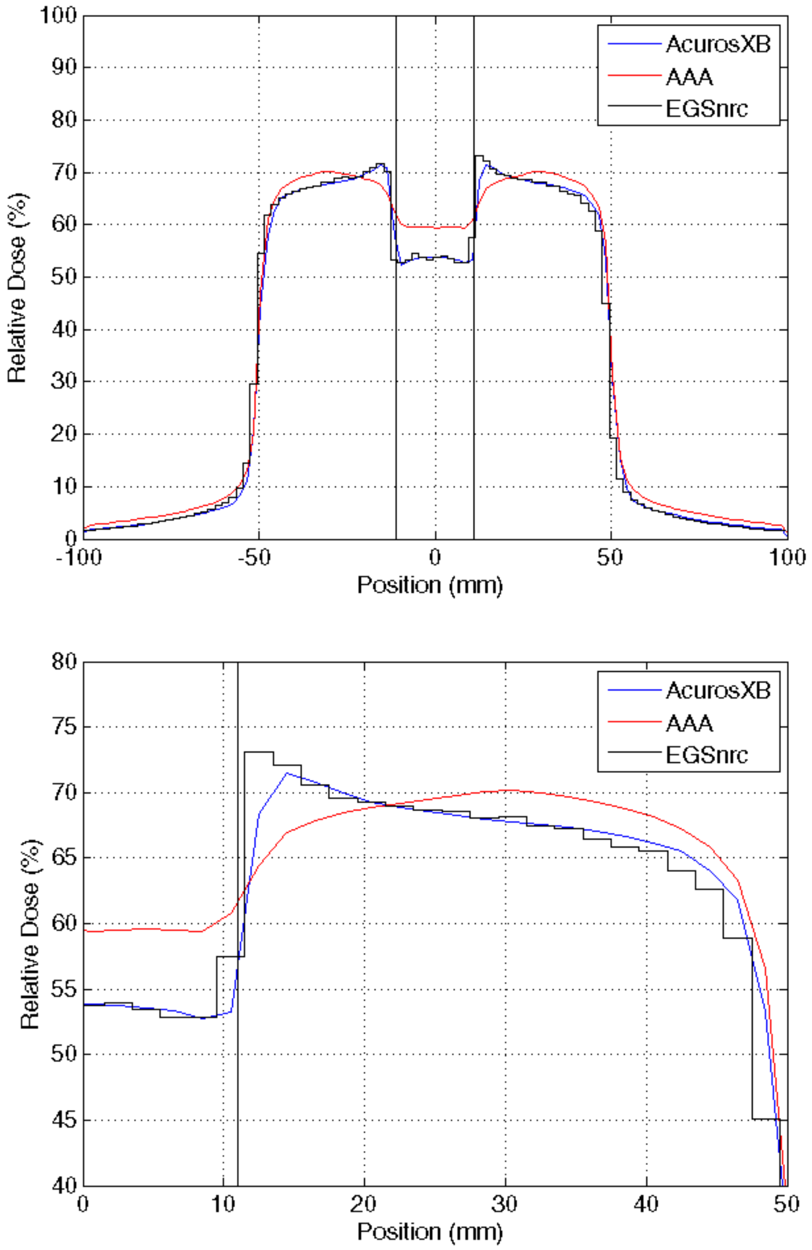

Figure 4.5: Dose profile plot for 6 MV photons through a 20x20x20 cm^3 skeletal muscle cube with a stainless steel centre (magnified on bottom). The vertical black lines indicate the high-density boundaries.

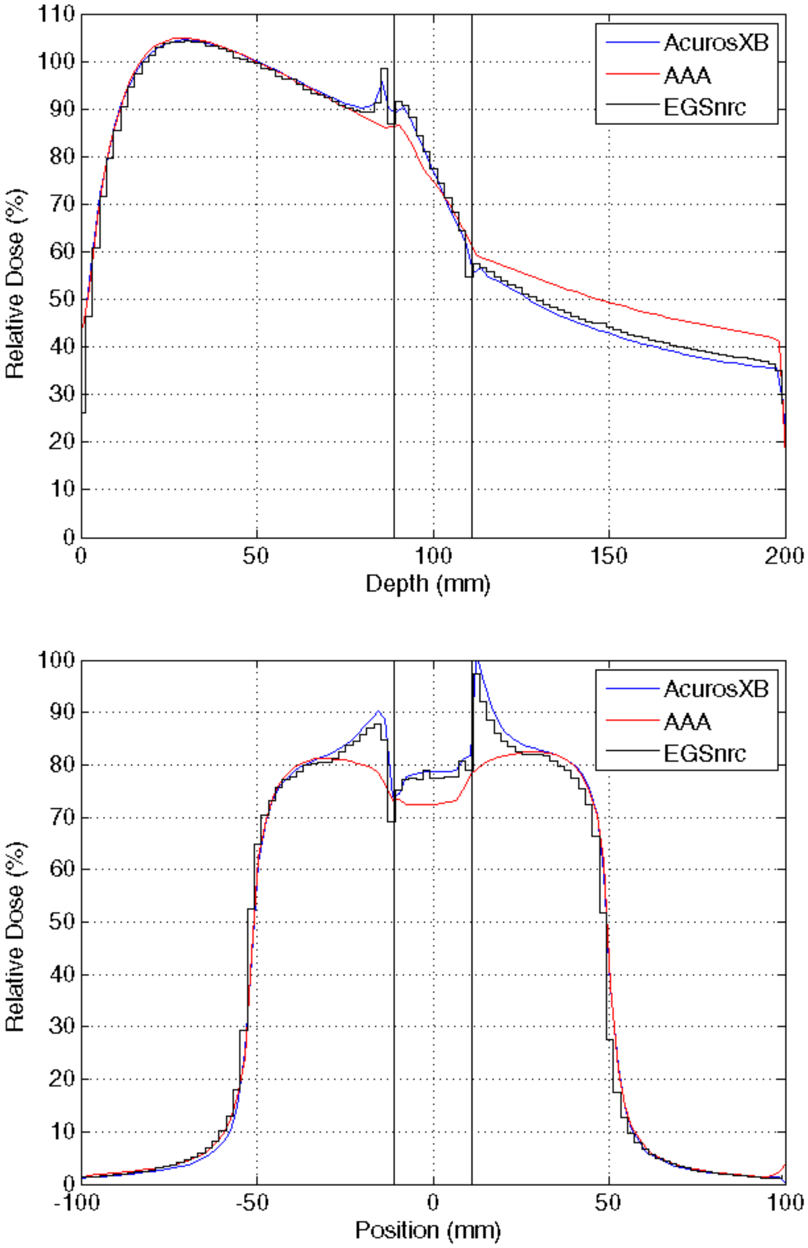

Figure 4.6: Depth dose (top) and dose profile (bottom) for 18 MV photons with a 10° gantry rotation through a 20x20x20 cm^3 skeletal muscle cube with a stainless steel centre. The vertical black lines indicate the high-density boundaries.

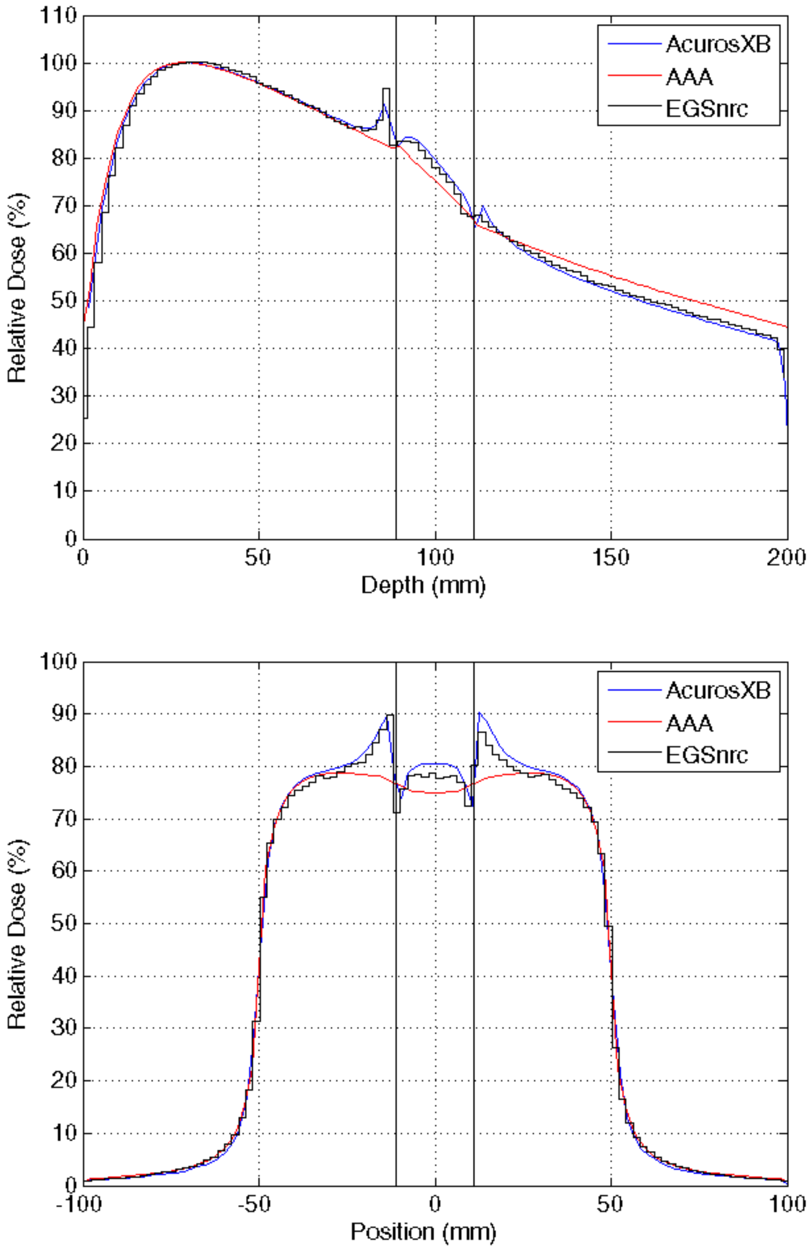

Figure 4.7: Depth dose plot for 18 MV photons through a 20x20x20 cm^3 skeletal muscle cube with a titanium alloy centre (magnified on bottom). The vertical black lines indicate the high-density boundaries.

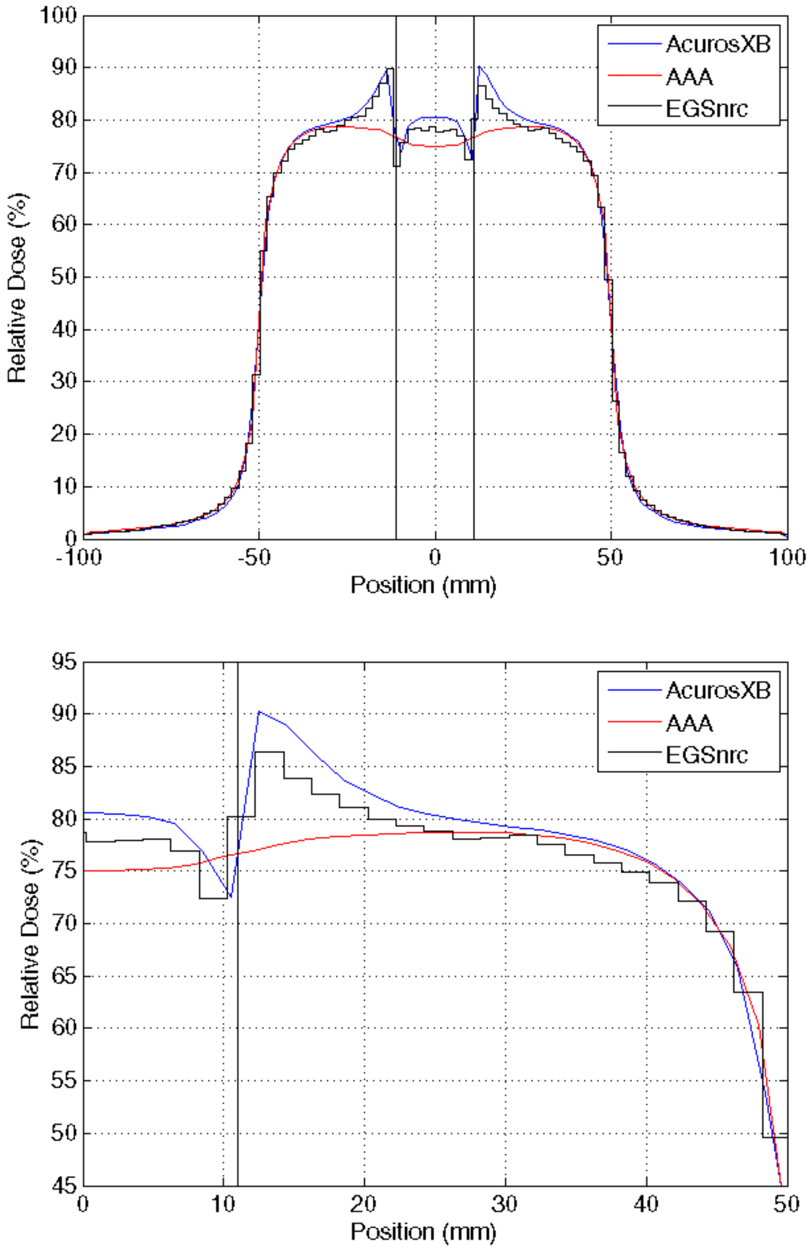

Figure 4.8: Dose profile plot for 18 MV photons through a 20x20x20 cm^3 skeletal muscle cube with a titanium alloy centre (magnified on bottom). The vertical black lines indicate the high-density boundaries.

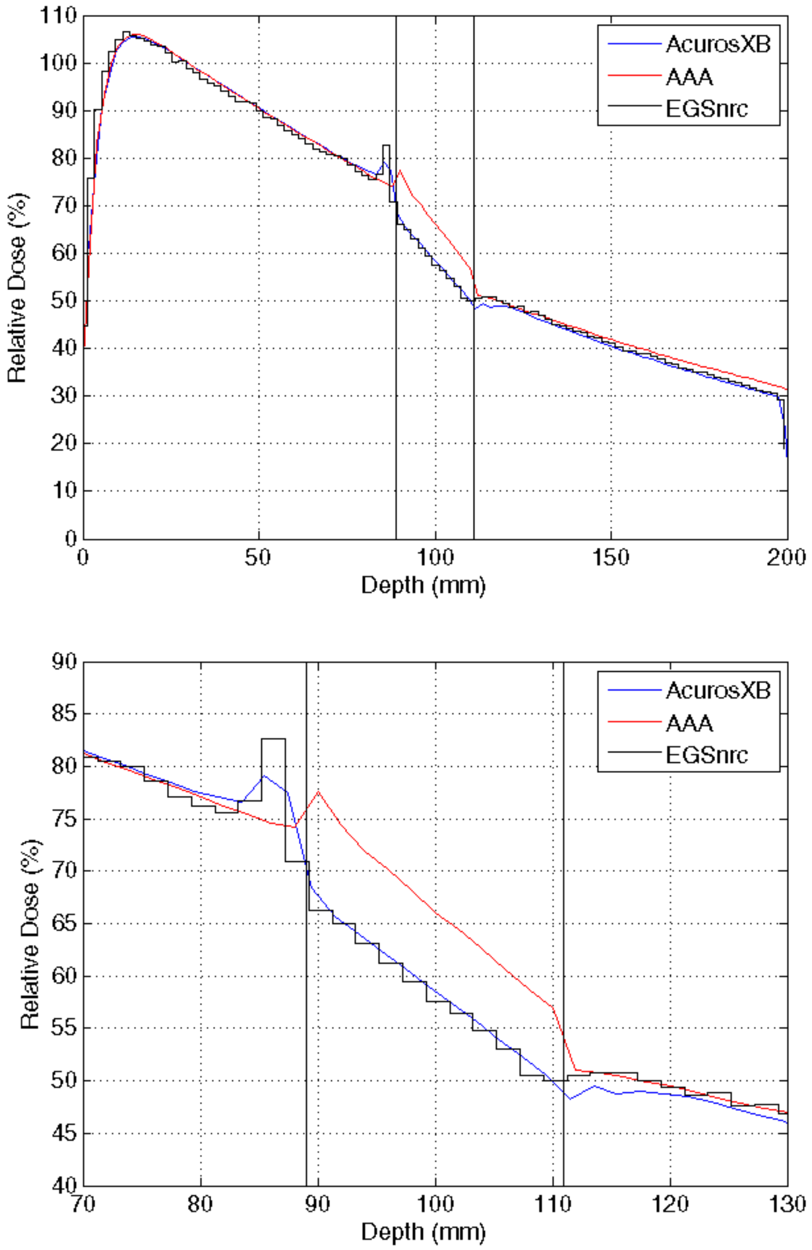

Figure 4.9: Depth dose plot for 6 MV photons through a 20x20x20 cm^3 skeletal muscle cube with a titanium alloy centre (magnified on bottom). The vertical black lines indicate the high-density boundaries.

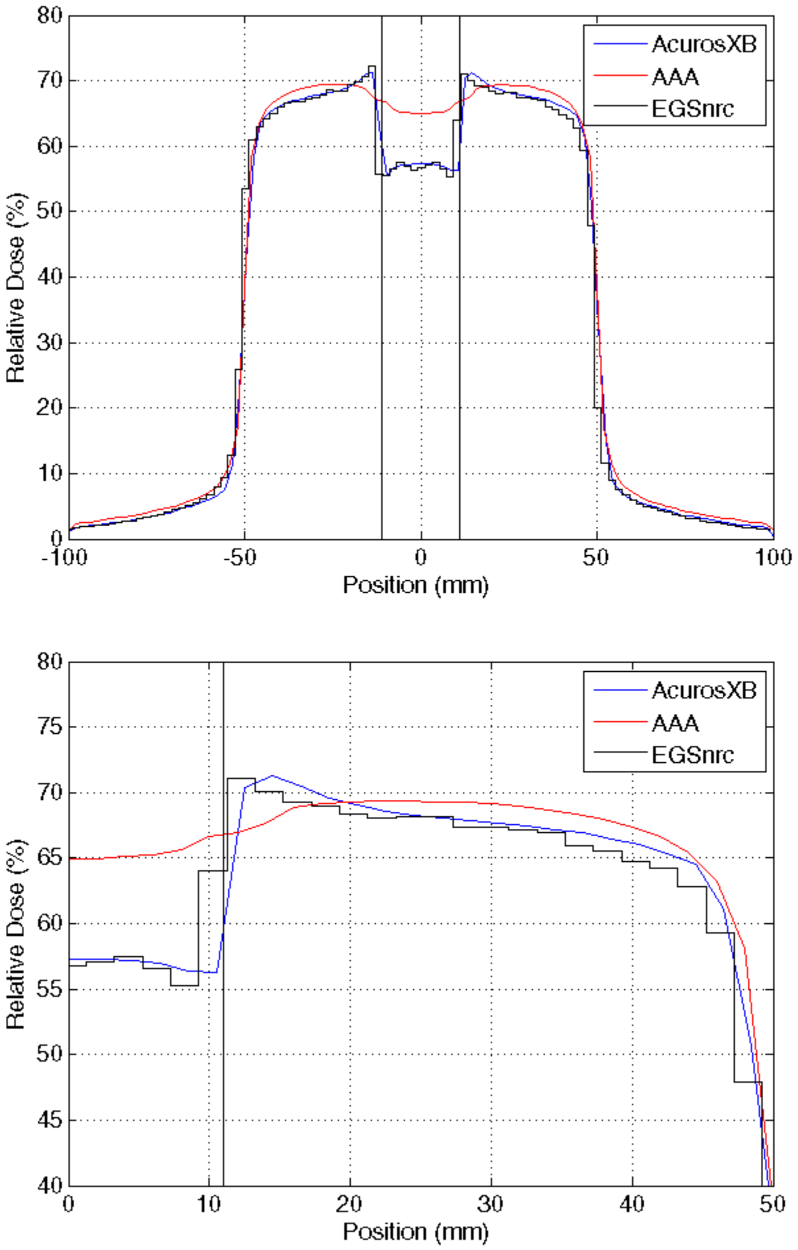

Figure 4.10: Dose profile plot for 6 MV photons through a 20x20x20 cm^3 skeletal muscle cube with a titanium alloy centre (magnified on bottom). The vertical black lines indicate the high-density boundaries.

Table 4.1: γ-analysis results for 20x20x20 cm^3 virtual phantoms at 2% and 2 mm as calculated by Acuros XB and AAA referenced against Monte Carlo. Results, in percent, are representative of those voxels containing at least half the maximum dose.

Geometry	Material	Energy (MV)	AcurosXB	AAA
On Axis	Steel	18	97.1	84.5
		6	98.7	84.7
	Titanium	18	96.8	87.2
		6	98.6	92.9
Oblique	Steel	18	97.3	60.9

Table 4.2 lists the magnitude and extent of each back- and lateral-scatter peak for 18 MV and 6 MV photons delivered on-axis through stainless steel and titanium alloy as calculated by Acuros XB and Monte Carlo. Monte Carlo uncertainties arise from the data's inherent statistical variance while Acuros XB uncertainties are estimated based on the change in dose value between adjacent voxels. AAA data is not included because, as can be seen in Figures 4.2–4.10, these features are either absent or incompatible for comparison as modeled by AAA. These properties, then, characterize the dose perturbations unaccounted for in current clinical planning techniques. Agreement between Acuros XB and Monte Carlo is generally very good, except for the heights of back-scatter peaks due to 6 MV photons in titanium alloy given as 11±2% and 6±1% as calculated by Monte Carlo and Acuros XB, respectively. It is possible, however, that this is a pixelation effect where the Monte Carlo back-scatter

Table 4.2: Characterization of back-scatter and lateral-scatter peaks due to stainless steel and titanium alloy inhomogeneities. Heights are given in percent of the unperturbed homogeneous dose.

Energy	Material	Model	Back Scatter Peak		Lateral Scatter Peak	
			Height (%)	Width (mm)	Height (%)	Width (mm)
18 MV	Stainless Steel	Monte Carlo	15±2	10±2	15±2	15±2
		Acuros XB	14±4	12±2	15±1	16±2
	Titanium Alloy	Monte Carlo	14±2	14±2	13±2	15±2
		Acuros XB	10±3	16±2	14±1	20±2
6 MV	Stainless Steel	Monte Carlo	12±2	7±2	7±2	13±2
		Acuros XB	9±2	9±2	5±1	16±2
	Titanium Alloy	Monte Carlo	11±2	5±2	5±2	14±2
		Acuros XB	6±1	5±2	5±1	14±2

peak exists in a single pixel over 2 mm while the Acuros XB back-scatter peak exists over two pixels and so its magnitude is averaged over 4 mm.

10x10x10 cm^3 Cubic Phantom

Figure 4.11 presents data for a 5x5 cm^2 field of 18 MV photons normal to the surface of the 10x10x10 cm^3 virtual phantom described in Section 3.3.1. The advantages of a smaller phantom are the ability to perform calculations on a smaller dose voxel grid and a closer investigation of interface and scatter effects. Even at a resolution of 0.1 cm in all directions, Acuros XB continues to show very good agreement with Monte Carlo in all of the features mentioned in the 20x20x20 cm^3 phantom case. Attenuation of the beam remains consistent between Acuros XB and Monte Carlo while AAA maintains an exit-dose offset between 5% and 10%. Due to reduced size, the data was normalized to 100% at 3 cm depth along the beam axis.

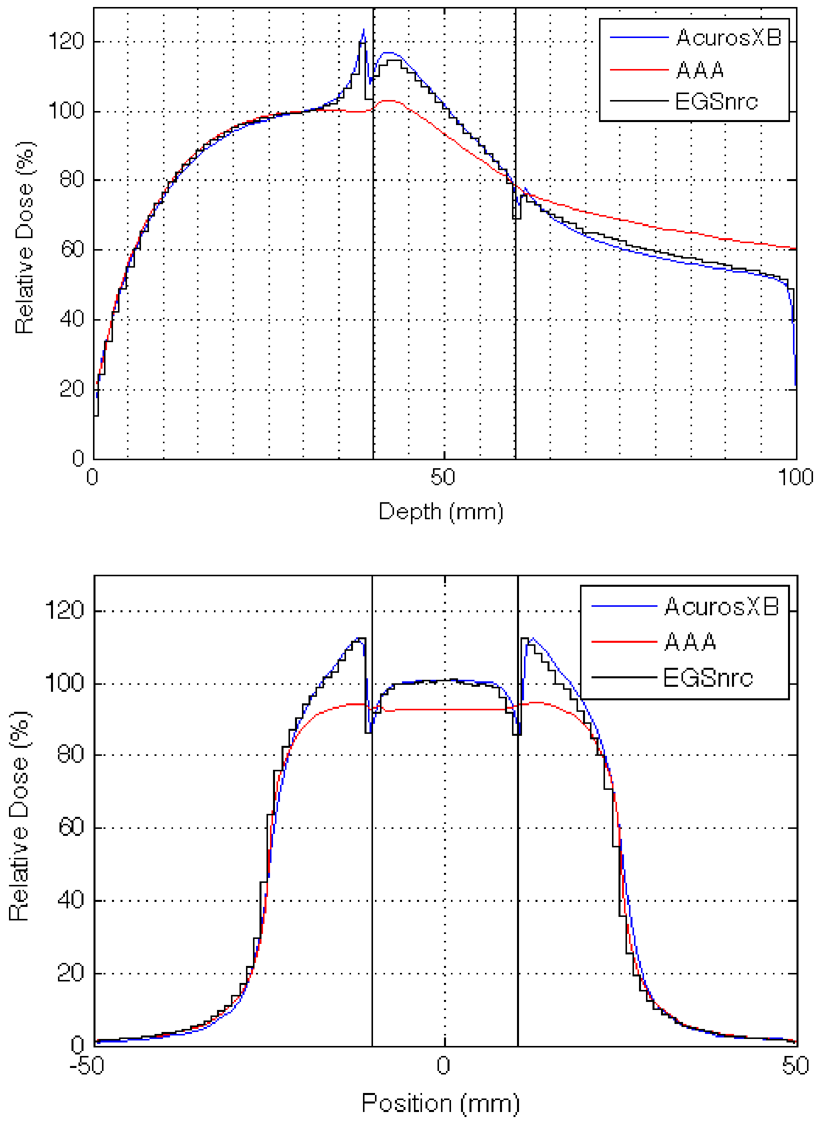

Figure 4.11: Depth dose (top) and dose profile (bottom) for 18MV photons through a 10x10x10 cm^3 skeletal muscle phantom with a stainless steel centre. The vertical black lines indicate the high-density boundaries.

4.3 Water Phantoms

Regular Geometry - Stainless Steel Rods

Figure 4.12 is an axial slice of a percent difference map and γ-factor distribution comparing Acuros XB and Monte Carlo for a calculations using the water tank phantom containing cylindrical stainless steel rods as outlined in Section 3.3.2. A 10x10 cm^2 field of 18 MV photons was positioned directly above one of the stainless steel rods to ensure complete coverage in the x-direction and delivery was simulated by Acuros XB, AAA and Monte Carlo. Dose is reported on a 0.2 cm grid in every direction. The colourmap in the top panel of Figure 4.12 corresponds to differences between Acuros XB and Monte Carlo within ±4%, or $\gamma = 2$ for a 2%, 0 mm γ-analysis. The bottom panel of Figure 4.12 is a γ-factor distribution corresponding to the associated difference colourmap. This γ-analysis was performed at 2 mm and 2% after normalizing the data by minimizing the sum of the squared differences between distributions using a least squares optimization. The comparative distributions for AAA are presented in Figure 4.13. A γ-analysis summary for Acuros XB and AAA referenced to Monte Carlo is included in Table 4.3.

Table 4.3: γ-analyses results for water phantoms at 2% and 2 mm as calculated by Acuros XB and AAA referenced against Monte Carlo. Results, in percent, are representative of those voxels containing at least half the normalized dose.

Geometry	Material	Energy (MV)	AcurosXB	AAA
Regular	Steel	18	95.1	88.3
		6	92.1	93.1
Irregular	Steel	18	97.2	85.8
		6	96.8	88.7
	Titanium	18	97.5	90.3
		6	97.1	92.5

Irregular Geometry - Hip Prostheses

A 10x10 cm^2 field of 18 MV photons normal to the surface of the water tank containing hip prostheses described in 3.3.2 was modeled in two arrangements. In each arrangement a field was positioned over either the steel or the titanium alloy prosthesis so that the high-density object was entirely covered by the field in the x-direciton.

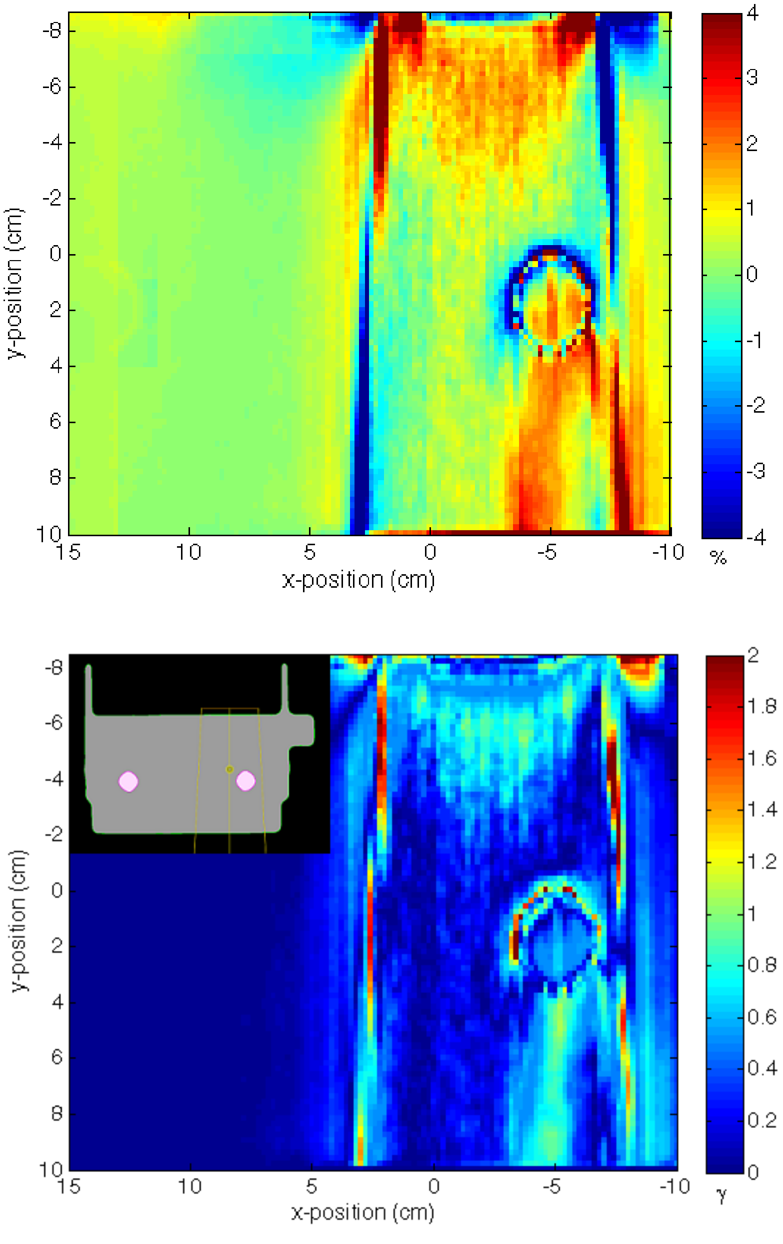

Figure 4.12: Percent dose difference (top) and γ-factor distribution (bottom) for 18 MV photons through a stainless steel rod as calculated by Acuros XB compared with Monte Carlo. Differences range between ±4% and the γ-analysis was done at 2% and 2mm.

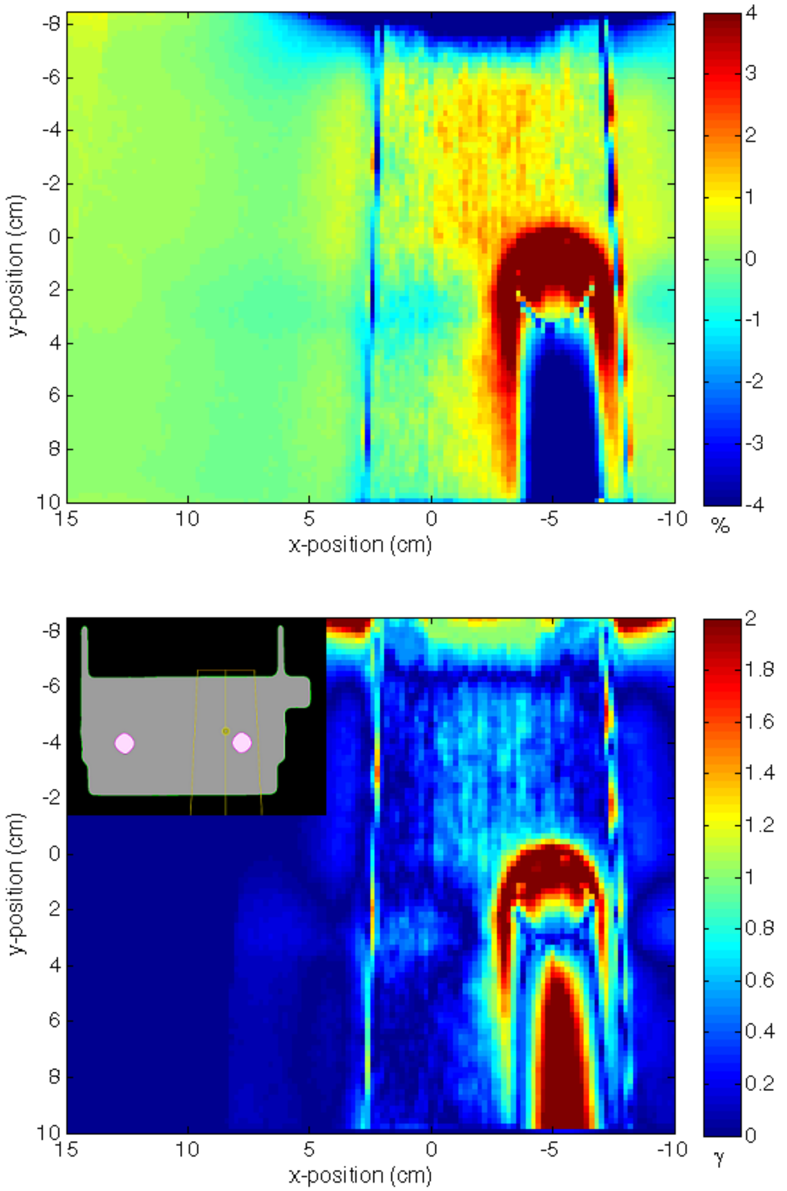

Figure 4.13: Percent dose difference (top) and γ-factor distribution (bottom) for 18 MV photons through a stainless steel rod as calculated by AAA compared with Monte Carlo. Differences range between ±4% and the γ-analysis was done at 2% and 2mm.

Calculations were performed by Acuros XB, AAA and Monte Carlo on a 0.2 cm dose grid in every direction. Dose distribution differences between Acuros XB and Monte Carlo for both arrangements are displayed in the top panels of Figures 4.14

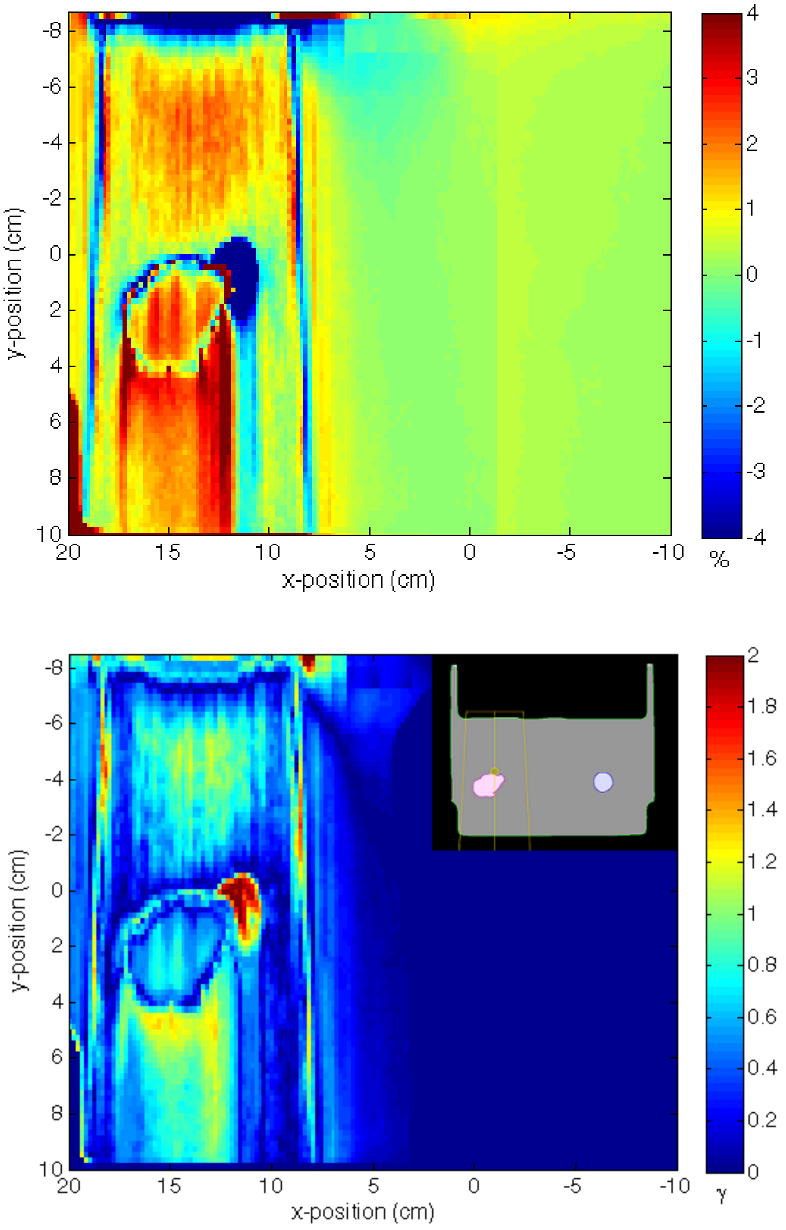

Figure 4.14: Percent dose difference (top) and γ-factor distribution (bottom) for 18 MV photons through a steel alloy hip prosthesis as calculated by Acuros XB compared with Monte Carlo. Differences range between ±4% and the γ-analysis was done at 2% and 2 mm.

and 4.15. Again, the differences displayed are between ±4%. The bottom panels of Figures 4.14 and 4.15 are the corresponding γ-factor distributions, evaluated for 2% and 2 mm. Figure 4.16 shows comparative γ-analyses for AAA data referenced

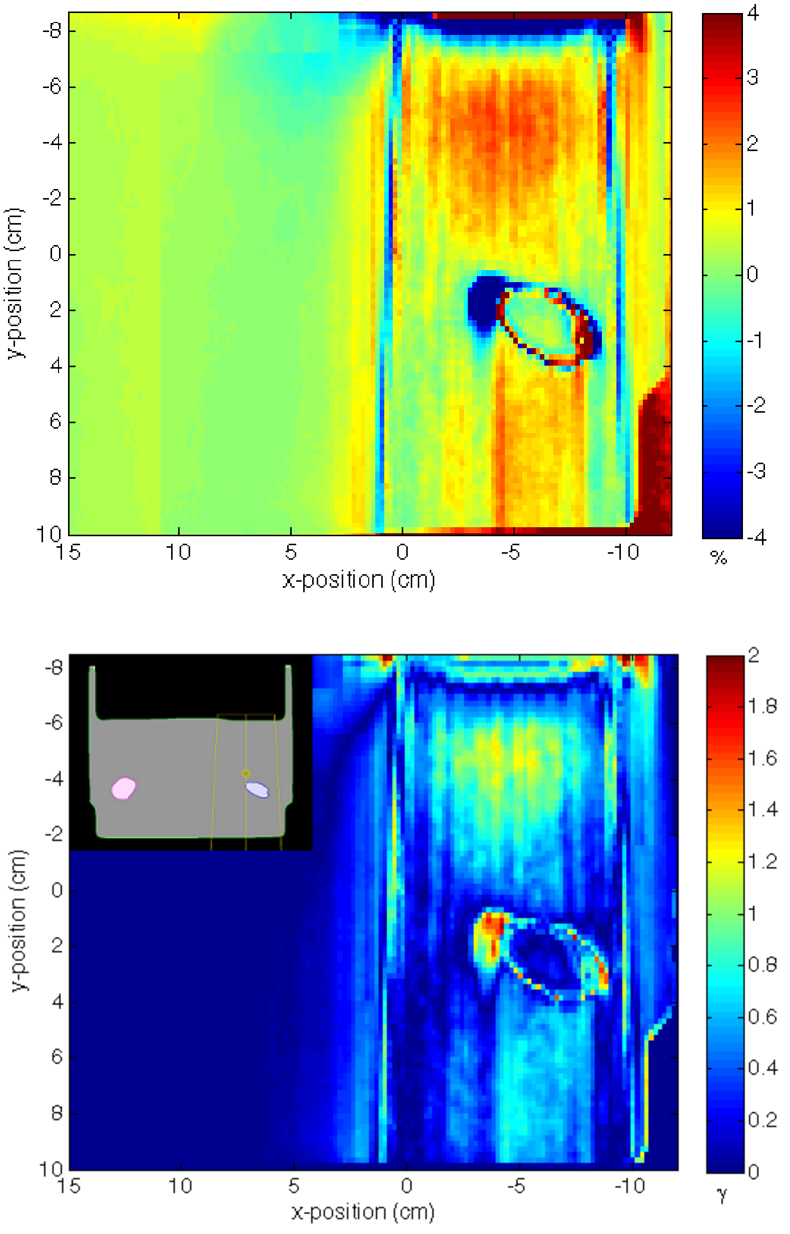

Figure 4.15: Percent dose difference (top) and γ-factor distribution (bottom) for 18 MV photons through a titanium alloy hip prosthesis as calculated by Acuros XB compared with Monte Carlo. Differences range between ±4% and the γ-analysis was done at 2 mm and 2%.

against Monte Carlo. A summary of γ-results is included in Table 4.3. Again, least squares minimization was used to determine a normalization factor before conducting the analyses.

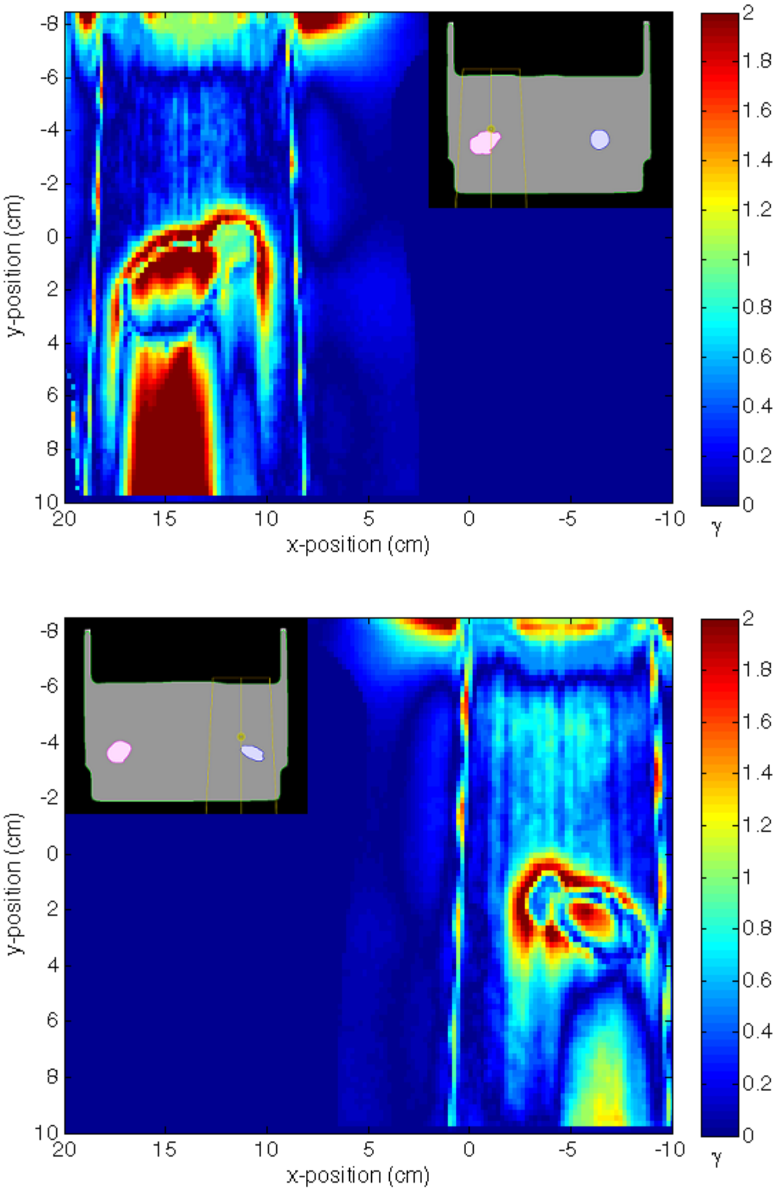

Figure 4.16: γ-factor distributions for 18 MV photons through steel (top) and titanium alloy (bottom) hip prostheses as calculated by AAA compared with Monte Carlo. γ-analysis were performed at 2 mm and 2%.

4.4 Patient Case

Figure 4.17 shows field arrangements for the first stage of a prostate treatment plan for a patient who received radiation therapy at VIC in February 2011. The plan was calculated using AAA and approved for delivery. As can be seen on the CT, the patient has a unilateral left hip prosthesis which necessitated modification of the

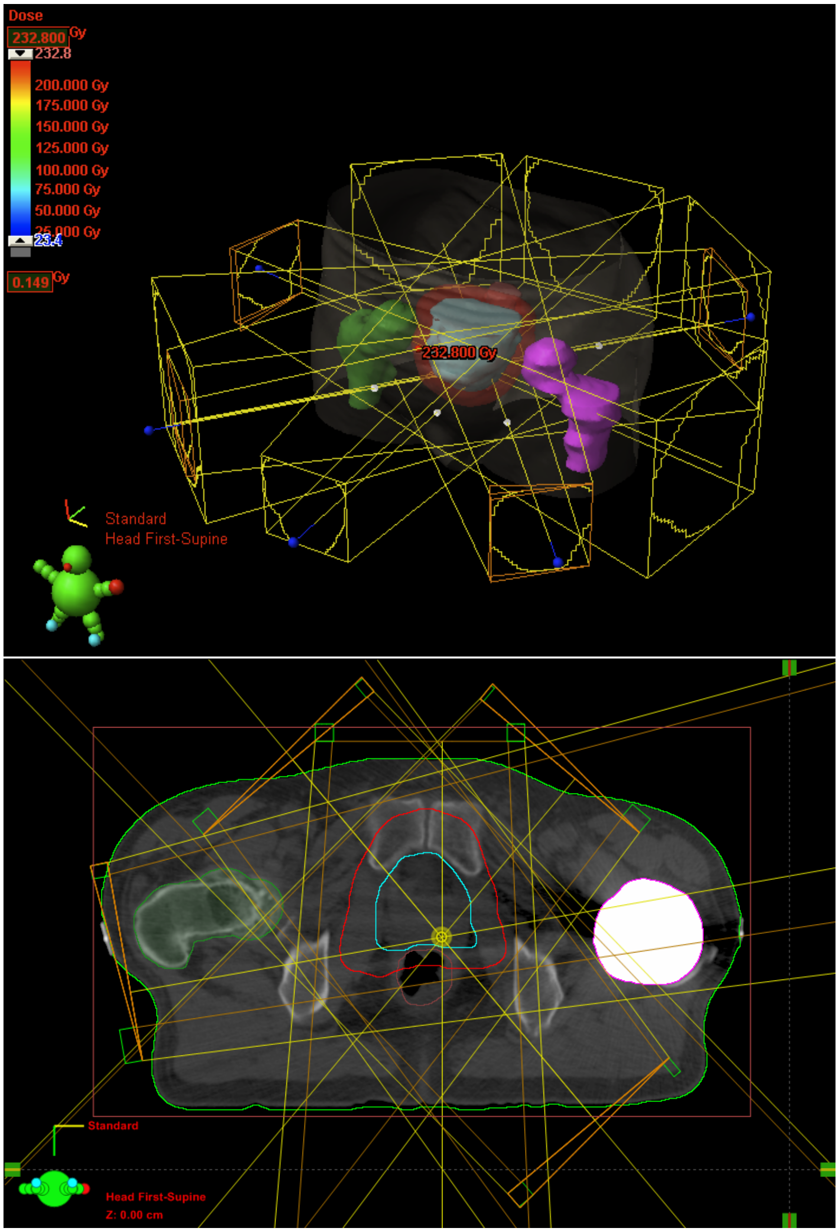

Figure 4.17: Treatment plan field arrangement for a prostate patient with a unilateral hip prosthesis.

optimal 5-field arrangement to avoid delivering radiation through the prosthesis. This modification includes passing the right-lateral field through the prosthesis, assuming that any errors in calculating the exit dose will not impact the calculated dose to the planned target volume. The AAA dose distribution is compared to Monte Carlo

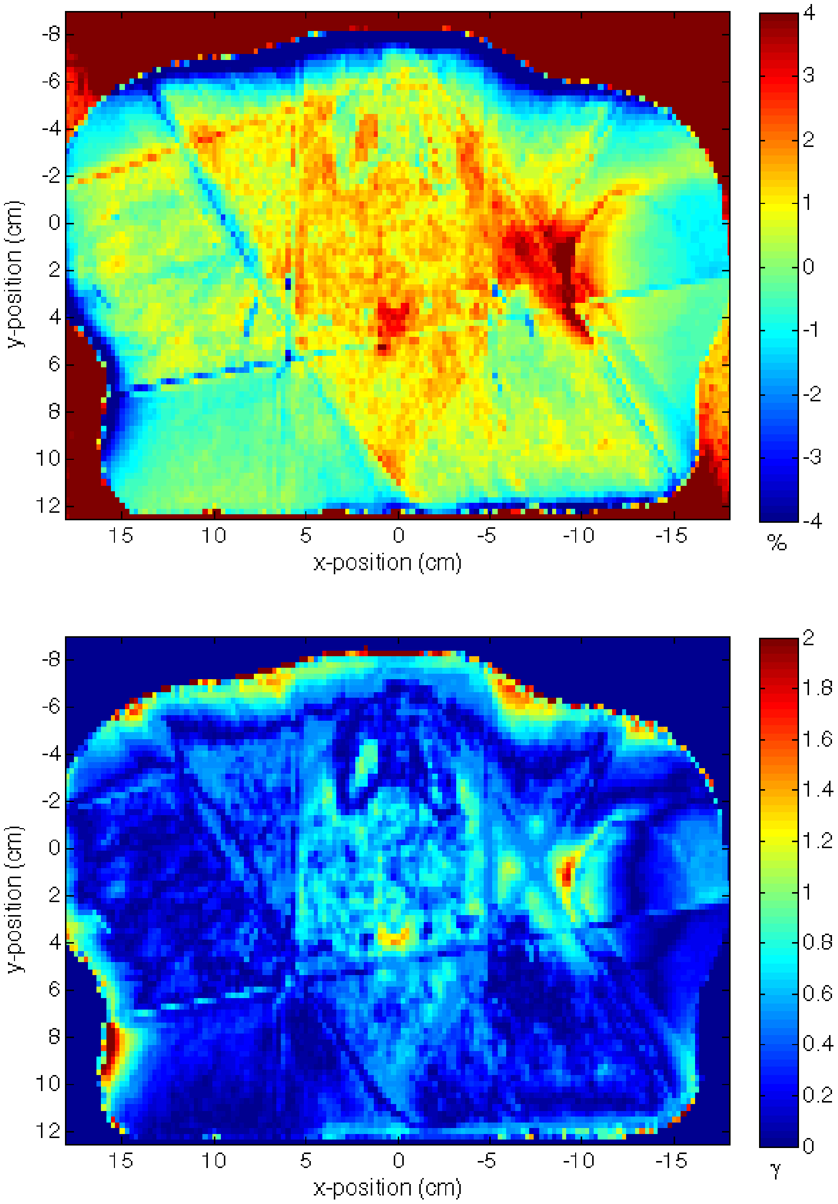

Figure 4.18: Percent dose difference (top) and γ-factor distribution (bottom) for a prostate treatment plan as calculated by AAA and Monte Carlo. The difference colourmap ranges between ±4% and the γ-analysis was done at 2% and 2 mm.

in Figure 4.18. The top image is a percent dose difference colourmap indicating differences between ±4%, or $\gamma = 2$ for a 2%, 0 mm analysis. There is large discrepancy outside of the body contour because Monte Carlo calculates dose outside the body while Eclipse algorithms do not. The bottom image is a γ-evaluation performed at

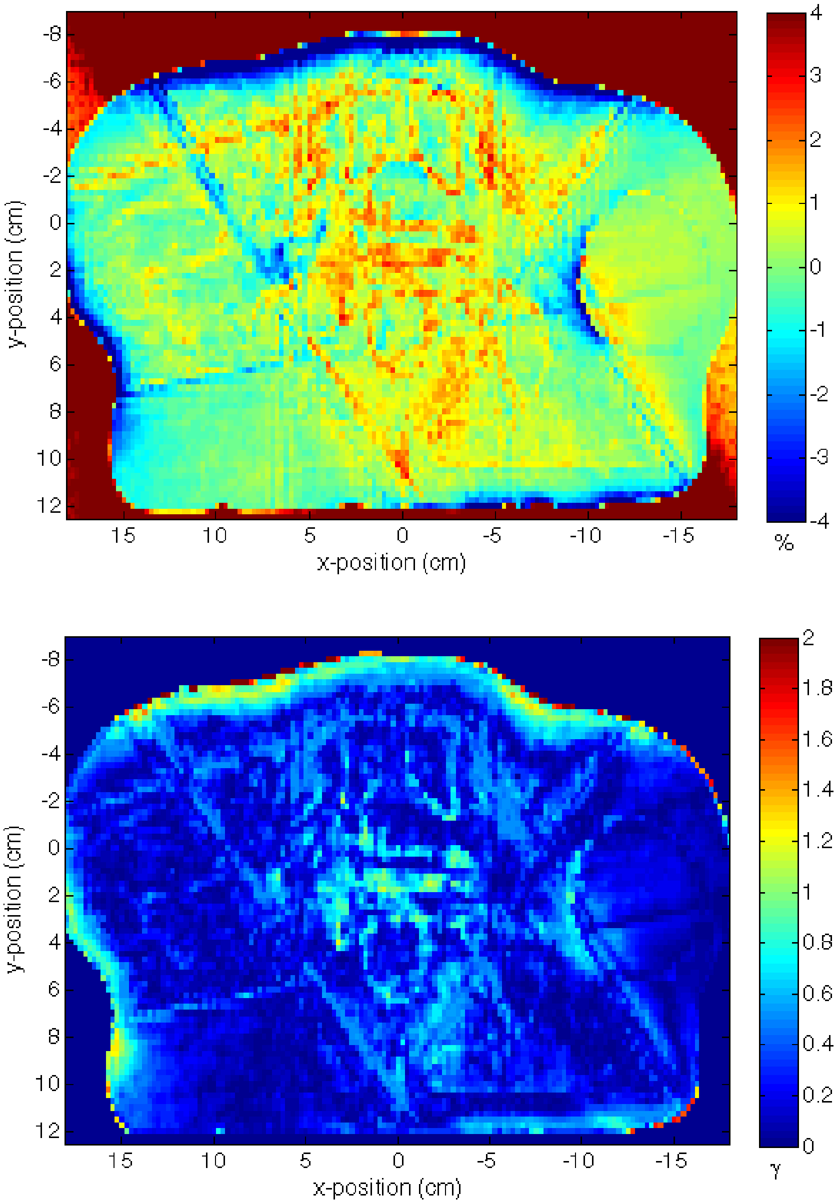

Figure 4.19: Percent dose difference (top) and γ-factor distribution (bottom) for a prostate treatment plan as calculated by Acuros XB and Monte Carlo. The difference colourmap ranges between ±4% and the γ-analysis was done at 2% and 2 mm.

2% and 2 mm after normalizing the data by a factor determined by least squares minimization. 97.0% of voxels containing at least 1% of the maximum dose were within γ-tolerance.

For this research, the treatment plan was recalculated using Acuros XB and compared with Monte Carlo. The resulting percent dose difference and γ-factor map are shown in Figure 4.19. The evaluations were performed in the same manner as indicated for the AAA, again subject to a normalization factor determined by least squares. 98.7% of voxels containing at least 1% of the maximum dose were within γ-tolerance. Even in this clinical case, where the presence of multiple fields is expected to minimize errors through averaging, Acuros XB still demonstrates improved accuracy on the inside surface of the hip prosthesis.

4.5 Computation time

The introduction of an algorithm with a comparable degree of accuracy to Monte Carlo has little advantage to radiotherapy planners unless it can be used at clinical time scales. The times required to calculate a selection of dose distributions using Monte Carlo, AAA and AcurosXB are displayed in Table 4.5. Monte Carlo calculations were performed on the 36 CPU cluster described in Section 3.1.1 while Acuros XB and AAA calculations were done with dual quad-core CPUs and 24 GB of 1066 MHz RAM.

Table 4.4: Computation times for Monte Carlo, AAA and Acuros XB

Calculation Volume (cm^3)	Field Size (cm^2)	Resolution (cm)	Energy (MV)	Calculation Time		
				MC	AAA	AXB
10x10x10	5x5	0.1	18	29.6 hrs	8 sec	6.8 min
			6	13.9 hrs	8 sec	4.9 min
20x20x20	10x10	0.2	18	38.9 hrs	12 sec	3.0 min
			6	15.6 hrs	5 sec	2.2 min

Chapter 5

Discussion of Results

Results of the film measurements outlined in Section 3.2 were presented and discussed in Section 4.1. The conclusion of this brief investigation is that the 30% forward-scatter dose peak presented in Figure 3.2 is not expected in measurements or accurate model calculations for 18 MV photons through a high-density inhomogeneity [11]. The focus of Chapter 5, then, shall be an evaluation of the experimental dose distribution data presented in Chapter 4 and the performance of Acuros XB in dealing with increased photon and electron scatter due to high-density objects.

A quantitative comparison of 3-D dose distributions can be a somewhat arbitrary exercise and there is no easy definition of a match as small differences in calculation results are often impossible to measure dosimetrically. Tools such as γ-analyses can be useful in providing a quantity that can be easily reported, but the significance of that value can be easily undermined by biased evaluation conditions: when 90% of a volume receives 0 Gy it is easy to report that your results have performed within γ-tolerance with 90% success. In an attempt to avoid such volume effects, the γ-analysis results tabulated in Chapter 4 include only those voxels containing at least half the maximum dose for virtual phantom calculations and half the normalized dose for water phantom calculations where the normalized dose was selected through a least squares minimization of the total difference between the data to be evaluated and Monte Carlo. In a patient case, any dose is significant when delivered to healthy tissue, so a 1% dose threshold was used to remove dose to air from the patient case analysis.

Substantial efforts were taken to eliminate systematic differences between data generated by Acuros XB and data generated by Monte Carlo. Material data and cross sections in Monte Carlo were made to match those used in Eclipse and both systems were configured to model the output of the same clinical linear accelerator used for treatment at VIC. Despite the best attempts, however, there were some elements of the input data that could not be made uniform between systems.

As discussed in Section 2.3.2, there can be up to a whole pixel offset in the same image or dose distribution depending on the spatial interpretation of a pixel's position by the software generating or displaying the data. Release notes from Varian Medical Systems regarding Eclipse algorithms have indicated that the position of a contour boundary may be incorrect by up to one calculation voxel as interpreted by Acuros XB. This sort of position offset may result in the corresponding offset of a back- or lateral-scatter peak, as is evident in the right lateral-peaks in Figures 4.2–4.6 and 4.11, and the left-lateral peaks in Figures 4.7 and 4.9.

The use of an adaptive mesh grid for calculations means that dose reported by Acuros XB has been interpolated onto a fixed grid which introduces averaging effects to the solution, and discretization of angle and energy introduces systematic error into the Acuros XB solution, although Eclipse documentation limits this error at 0.1%. In a Monte Carlo calculation, the implication of simulating a finite number of particles is a degree of uncertainty in the final result. The Monte Carlo calculations performed here have, on average, 1–2% standard deviation in the final dose distributions, producing a noisy signal compared to Acuros XB and AAA and further reducing the significance of a voxel by voxel difference. These, and the limitations listed above should all be considered throughout the evaluation of Acuros XB that follows.

5.1 Virtual Phantoms

The purpose of investigating a geometrically ideal, virtual phantom is to reduce potential sources of variation and determine if an algorithm is capable of treating the simplest scenario accurately. Failure at this level might preclude any further investigation. A preliminary, qualitative overview of the dose distribution data presented in Figures 4.2 and 4.11 of the 20x20x20 cm^3 and 10x10x10 cm^3 virtual phantoms, respectively, indicates that Acuros XB is capable of accurately modeling the increase in electron scatter due to the presence of a high-density object. Acuros XB data shows appropriate dose peaks at the entrance and lateral surfaces of the high-density region as expected, and as predicted by Monte Carlo data.

Continuing qualitatively, consider the oblique field delivery presented in Figure 4.6. This calculation was performed to determine the effect, if any, of non-normal photon incidence on the accuracy of scatter modeling by Acuros XB. From these depth dose and dose profile samples it appears that interface orientation has very little, if any impact on the algorithm's accuracy. The same conclusions can be drawn for the variant cases presented in Figures 4.4–4.9 which include 6 MV photons and titanium alloy inhomogeneities.

The quantitative analysis summarized in Table 4.1 presents an interesting picture of algorithm performance. The γ-analyses parameters used, 2% and 2 mm, were chosen to be representative of expected uncertainty bounds: 2 mm is the dimension of a single dose voxel while 2% represents a reasonable bound on Monte Carlo data variance. In comparison with Monte Carlo, Acuros XB is within γ-tolerance for greater than 96.5% of voxels considered in all cases. In contrast, the highest γ-success percentage for AAA is 92.9% while its worst agreement, in the case of the obliquely delivered field, is 60.9%. Overall, these results suggest Acuros XB to be better equipped to deal with high-density volumes than AAA.

5.2 Water Phantoms

Generally, agreement between Acuros XB and Monte Carlo is similar for the water phantom and the virtual phantom calculations. A summary of γ-analysis results is presented in Table 4.3. Acuros XB γ-tolerances range from 92% of voxels considered in the case of a 6 MV field through a cylindrical stainless steel rod, to 97.5% of voxels considered for an 18 MV field through a titanium alloy prosthesis. AAA γ-analysis results for the same set of calculations range from 85.8% in the case of an 18 MV field through a steel alloy prosthesis to a maximum of 93.13% in the case of a 6 MV field through a cylindrical stainless steel rod.

The increase of geometric complexity in the water phantom cases, as well as the reduction of contour quality with the introduction of image noise suggests an increased degree of variance between calculation results. The uncertainty in boundary definition combined with variations in boundary interpretation may very well account for a majority of discrepancies between Acuros XB and Monte Carlo. Referring to the difference maps in Figures 4.12, 4.14 and 4.15, regions of disagreement tend to exist primarily at the phantom surface and at high-density interfaces, all of which are subject to the listed sources of variation.

5.3 Patient Case

Because a clinical treatment plan often contains multiple fields with unique shapes delivered from various angles, differences in dose distributions between algorithms are expected to be somewhat washed or averaged out. Attempting to identify a modeling flaw as the source of a dose discrepancy is better suited to the phantom cases discussed in preceding sections. The purpose of this clinical case is to illustrate the impact of modeling shortfalls and strengths in a clinical environment.

Figure 4.18 shows the discrepancies between AAA and Monte Carlo for the treatment fields shown in Figure 4.17. A γ-analysis of these distributions shows a 97.0% agreement at 2% and 2 mm for those voxels containing at least 1% of the normalized dose. This is an excellent success rate, however, from an axial slice of the dose-difference, AAA clearly demonstrates an underestimate of dose on the inside surface of the prosthesis, represented in the dose difference plot by a region of dark red and a smaller region of red in the γ-factor plot. This is a region of the metal structure that likely has contact with bone, and depending on the severity of that underestimate, this could lead to a radiation induced break or a secondary cancer.

The same difference map for Acuros XB is displayed in Figure 4.19 and there are no comparable hot or cold spots. The γ-analysis results for the Acuros XB data show 98.7% of voxels containing at least 1% of the normalized dose to be within tolerance. This is an improvement over AAA, even if it is a quantitatively slight one. In terms of target volume coverage and critical volume sparing there is little difference between Acuros XB and AAA, but the absence of localized over- or under-dosage as represented by Acuros XB is a significant result for clinical work and an advantageous improvement for dosimetrists and oncologist planning around hip prostheses.

5.4 Summary

Overall, the preceding analyses have shown Acuros XB to be in better agreement with Monte Carlo than AAA for dose calculations involving high-density volumes. The magnitudes and extents of back- and lateral-scatter peaks are similar for Acuros XB and Monte Carlo, and γ-analysis results are better for Acuros XB than for AAA when evaluated against Monte Carlo. In addition, previously published data suggesting the existence of a 30% forward-scatter peak has been discredited by film measurement. In Chapter 6, the final chapter of this thesis, the implications of these findings and remaining considerations are discussed.

Chapter 6

Conclusions & Considerations

The purpose of this research is to determine whether the solutions presented by Acuros XB hold true to the physical principles governing radiation transport after the introduction a high-density inhomogeneity to the calculation volume. It is not within the scope of this project to conclude that Acuros XB is or is not acceptable for clinical use. The clinical commissioning and implementation of a novel algorithm is left to the medical physicists guiding and evaluating this work.

The first successful result for Acuros XB was the qualitative match with film measurements taken for 18 MV photons through a high-density slab geometry, featuring a sharp backscatter peak on the proximal surface of the inhomogeneity and the absence of a forward scatter peak on its distal surface. Considering the position and calibration uncertainties associated with the measured data but not accounted for in the plotted error bars and the boundary definition uncertainty associated with calculated data, this might also be considered a quantitative success, as the discrepancies between Acuros XB and measured data are between 0.7 and 3.3% away from the high-density boundaries. The agreement between measured and Monte Carlo data is even better, ranging between 0.03 to 1.6% away from the boundaries.

The next positive result was in the modeling of lateral scatter from the high-density region demonstrated by the virtual phantom calculations. This effect was not accurately reflected in AAA data and may prove too difficult to be handled by a convolution-superposition algorithm. Acuros XB was able to consistently match its lateral peaks and other perturbation features with those modeled by Monte Carlo, regardless of beam angle, energy or complexity of the high-density contour.

γ-analysis pass statistics, which were in excess of 95% in all but one case when performed at 2% and 2 mm constraints, strongly suggest an algorithm capable of reflecting the physics of radiation transport as accurately as Monte Carlo. The differences that do exist between Acuros XB and Monte Carlo, for the most part, would be nearly impossible to measure dosimetrically. In fact, when these tiny effects are added up in a typical treatment plan they nearly vanish, as demonstrated by the 98.7% γ-analysis pass statistic for the prostate plan examined. Not only does Acuros XB perform with accuracy comparable to Monte Carlo, it does so at time scales entirely appropriate for a clinical planning, making it eligible for clinical consideration.

The implementation of a calculation algorithm such as Acuros XB would not change the way dosimetrists and oncologist plan treatments for patients with hip prostheses, rather, it would increase the confidence with which they do so. Regardless of the accuracy with which one can predict the dose distribution in and around a high-density object, the resulting dose shadow means that treating through a prosthesis is an ineffective means of dose delivery and will increase the dose required to treat the target volume to prescription, as well as increase the dose delivered to tissue adjacent to the prosthesis. If this were not enough, variability in day-to-day positioning of the patient on the treatment couch adds the risk of misaligning the prosthesis and overdosing everything beyond it. Instead, the implementation of an algorithm like Acuros XB would allow for better informed treatment planning, eliminating the uncertainty currently associated with planning around high-density regions.

Accuracy in modeling photon and electron scatter due to a high-density object is only part of the challenge involved in planning for such cases. Considering Figure 1.2 and the discussion of artifacts in Section 2.3.1, there remains a loss of density information due to the high-density region. CT shadows are often contoured and assigned appropriate tissue-equivalent properties, but streaks are difficult to negate and a contoured CT is still an approximation of reality. Techniques to correct high-density artifacts, such as CT post-processing and multimodal imaging, are still in development stage, and until they have been sufficiently validated for wide spread use, a degree of approximation will remain in pelvic treatment planning around prostheses.

Overall, Acuros XB has been shown to perform as well as Monte Carlo for modeling a dose distribution subject to increased photon and electron scatter due to the presence of a high-density object. Until now, there has not been a clinically appropriate algorithm available for such calculations. AAA, while acceptable for most radiotherapy planning cases, has shown deficiencies in its ability to accurately reflect the full extent of the dose perturbations that result from increased photon and electron scatter within a high-density volume. Once properly approved and commissioned for clinical use, Acuros XB will be an important tool for planners dealing with high-density implants.

Appendix A

Material Information

Table A.1: Material compositions for EGSnrc and Acuros XB.

Material	Element	Weight Fraction	
		EGSnrc	AcurosXB
Air	C	0.000124	
	N	0.7552	0.755268
	O	0.2318	0.231781
	Ar	0.01283	0.012827
Lung	H	0.1030	0.101278
	C	0.105	0.102310
	N	0.031	0.028650
	O	0.749	0.757072
	Na	0.002	0.00184
	Mg	-	0.00073
	P	0.002	0.0008
	S	0.003	0.00225
	Cl	0.003	0.00266
	K	0.002	0.001940
	Fe	-	0.00037
	Zn	-	0.00001

Table A.1: (continued)

Material	Element	Weight Fraction EGSnrc	 AcurosXB
Skeletal Muscle	H	0.100637	
	C	0.10783	
	N	0.02768	
	O	0.754773	
	Na	0.00075	
	Mg	0.00019	
	P	0.0018	
	S	0.00241	
	Cl	0.00079	
	K	0.00302	
	Ca	0.00003	
	Fe	0.00004	
	Zn	0.00005	
Light Bone	H	0.085	0.096
	C	0.404	0.099
	N	0.028	0.022
	O	0.367	0.744
	Na	0.001	0.005
	Mg	0.001	-
	P	0.034	0.022
	S	0.002	0.009
	Cl	0.002	0.003
	K	0.001	-
	Ca	0.074	-
	Fe	0.001	-

Table A.1: (continued)

Material	Element	Weight Fraction	
		EGSnrc	AcurosXB
Bone	H	0.047234	
	C	0.14433	
	N	0.04199	
	O	0.446096	
	Mg	0.0022	
	P	0.10497	
	S	0.00315	
	Ca	0.20993	
	Zn	0.0001	
Titanium Alloy	Ti	0.9	
	Al	0.06	
	V	0.04	
Stainless Steel	C	0.0008	
	Si	0.01	
	P	0.00045	
	Cr	0.19	
	Mn	0.02	
	Fe	0.68375	
	Ni	0.095	

Bibliography

[1] C. C. S. S. C. on Cancer Statistics, "Canadian cancer statistics 2011," Totonto, ON, 2011.

[2] M. Joiner and A. van der Kogel, eds., *Basic Clinical Radiobiology.* London: Hodder Arnold, 4th ed., 2009.

[3] O. N. Vassiliev, T. A. Wareing, J. McGhee, G. Failla, M. R. Salehpour, and F. Mourtada, "Validation of a new grid-based Boltzmann equation solver for dose calculation in radiotherapy with photon beams," *Phys Med Biol*, vol. 55, pp. 581–98, Feb 2010.

[4] A. Clark, "The effect of the Roentgen Rays in a case of chronic carcinoma of the breast," *British Medical Journal*, vol. 1, no. 2110, p. 1398, 1901.

[5] F. M. Khan, *The Physics of Radiation Therapy.* Philadelphia, PA: Lippincott Williams & Wilkins, 3rd ed., 2003.

[6] D. Thwaites and J. Tuohy, "Back to the future: the history and development of the clinical linear accelerator," *Phys Med Biol*, vol. 51, p. R343, 2006.

[7] W. Meredith, "40 years of development in radiotherapy," *Phys Med Biol*, vol. 29, p. 115, 1984.

[8] H. E. Johns and J. R. Cunningham, *The Physics of Radiology.* Springfield, Illinois: Thomas, 4th ed., 1983.

[9] P. Litt, "Photon Finish: The Race to Build the Bomb," Jun 2002.

[10] F. H. Attix, *Introduction to Radiological Physics and Radiation Dosimetry.* Weinheim, Germany: Wiley-VCH Verlag GmbH & Co., 2004.

[11] C. Reft, R. Alecu, I. Das, B. Gerbi, P. Keall, and E. Lief, "Dosimetric considerations for patients with HIP prostheses undergoing pelvic irradiation. Report of the AAPM Radiation Therapy Committee Task Group 63 prostheses undergoing pelvic irradiation. Report of the AAPM Radiation Therapy Committee Task Group 63," *Med. Phys.*, vol. 30, pp. 1162–1182, Jan 2003.

[12] K. A. Gifford, J. L. Horton, T. A. Wareing, G. Failla, and F. Mourtada, "Comparison of a finite-element multigroup discrete-ordinates code with Monte Carlo for radiotherapy calculations," *Phys Med Biol*, vol. 51, pp. 2253–2265, Apr 2006.

[13] K. Bush, I. M. Gagne, S. Zavgorodni, W. Ansbacher, and W. Beckham, "Dosimetric validation of Acuros® XB with Monte Carlo methods for photon dose calculations," *Med. Phys.*, vol. 38, no. 4, p. 2208, 2011.

[14] T. Han, J. K. Mikell, M. Salehpour, and F. Mourtada, "Dosimetric comparison of Acuros XB deterministic radiation transport method with Monte Carlo and model-based convolution methods in heterogeneous media," *Med. Phys.*, vol. 38, p. 2651, Jan 2011.

[15] I. Gagne and S. Zavgorodni, "Evaluation of the analytical anisotropic algorithm (AAA) in an extreme water-lung interface phantom using Monte Carlo dose calculations," *Journal of Applied Clinical Medical Physics*, vol. 8, no. 1, 2006.

[16] C. M. Bragg and J. Conway, "Dosimetric verification of the anisotropic analytical algorithm for radiotherapy treatment planning," *Radiother Oncol*, vol. 81, pp. 315–23, Dec 2006.

[17] I. J. Das and F. M. Kahn, "Backscatter dose perturbation at high atomic number interfaces in megavoltage photon beams," *Med. Phys.*, vol. 16, pp. 367–75, Jan 1989.

[18] R. D. Evans, *The Atomic Nucleus.* New York, New York: McGraw-Hill, 1955.

[19] M. Woo and J. Cunningham, "The validity of the density scaling method in primary electron transport for photon and electron beams," *Med. Phys.*, vol. 17, pp. 187–194, 1990.

[20] W. Ulmer, J. Pyyry, and W. Kaissl, "A 3D photon superposition/convolution algorithm and its foundation on results of Monte Carlo calculations," *Phys Med Biol*, vol. 50, pp. 1767–90, Apr 2005.

[21] G. M. Kremer, *An Introduction to the Boltzmann Equation and Transport Processes in Gases.* Berlin, Germany: Springer-Verlag Berlin Heidelberg, 2010.

[22] I. Kawrakow and A. Bielajew, “On the representation of electron multiple elastic-scattering distributions for Monte Carlo calculations,” *Nucl. Instrum. Methods B*, vol. 134, no. 3-4, pp. 325–336, 1998.

[23] R. Koch and R. Becker, “Evaluation of quadrature schemes for the discrete ordinates method,” *J. Quant. Spectros. Radiat. Transfer*, Jan 2004.

[24] J. T. Bushberg, J. A. Seibert, E. M. Leidholdt, and J. M. Boone, *The Essential Physics of Medical Imaging.* Philadelphia, PA: Lippincott Williams & Wilkins, 2nd ed., 2002.

[25] J. Wei, G. Sandison, W. Hsi, M. Ringor, and X. Lu, “Dosimetric impact of a CT metal artefact suppression algorithm for proton, electron and photon therapies,” *Phys Med Biol*, Jan 2006.

[26] M. Aubin, O. Morin, J. Chen, and A. Gillis, “The use of megavoltage cone-beam CT to complement CT for target definition in pelvic radiotherapy in the presence of hip replacement,” *British Journal of Radiology*, Jan 2006.

[27] A. Niroomand-Rad, C. Blackwell, B. Coursey, K. Gall, J. Galvin, W. McLaughlin, A. Meigooni, R. Nath, J. Rodgers, and C. Soares, “Radiochromic film dosimetry: recommendations of AAPM radiation therapy committee task group 55,” *Med. Phys.*, vol. 25, pp. 2093–2115, 1998.

[28] I. Kawrakow, D. Rogers, F. Tessier, and B. Walters, “The EGSnrc code system: Monte Carlo simulation of electron and photon transport,” Tech. Rep. PIRS-701, National Research Council of Canada, Ottawa, Canada, 2010.

[29] B. Walters, I. Kawrakow, and D. Rogers, “DOSXYZnrc users manual,” Tech. Rep. PIRS-794revB, Ottawa, Canada, 2009.

[30] D. Rogers, B. Walters, and I. Kawrakow, “BEAMnrc users manual,” Tech. Rep. PIRS-0509(A)revL, National Research Council of Canada, Ottawa, Canada, 2009.

[31] G. Cranmer-Sargison, W. Beckham, and I. Popescu, “Modelling an extreme water–lung interface using a single pencil beam algorithm and the Monte Carlo method,” *Phys Med Biol*, vol. 49, p. 1557, 2004.

[32] D. A. Low, W. B. Harms, S. Mutic, and J. A. Purdy, “A technique for the quantitative evaluation of dose distributions,” *Med. Phys.*, vol. 25, pp. 656–61, May 1998.